AFRL-AFOSR-JP-TR-2024-0031

The effects of freestream and kinematic perturbations on oscillating wings at low Reynolds numbers

Sridhar Ravi
University of New South Wales-NEW NCAGE Code
HIGH STREET
KENSINGTON, NSW, ,
AU

12/18/2023
Final Technical Report

Air Force Research Laboratory
Air Force Office of Scientific Research
Asian Office of Aerospace Research and Development
Unit 45002, APO AP 96338-5002

REPORT DOCUMENTATION PAGE

PLEASE DO NOT RETURN YOUR FORM TO THE ABOVE ORGANIZATION.

1. REPORT DATE	2. REPORT TYPE	3. DATES COVERED	
20231218	Final	START DATE 20200930	END DATE 20220929

4. TITLE AND SUBTITLE
The effects of freestream and kinematic perturbations on oscillating wings at low Reynolds numbers

5a. CONTRACT NUMBER	5b. GRANT NUMBER	5c. PROGRAM ELEMENT NUMBER
	FA2386-20-1-4084	
5d. PROJECT NUMBER	**5e. TASK NUMBER**	**5f. WORK UNIT NUMBER**

6. AUTHOR(S)
Sridhar Ravi

7. PERFORMING ORGANIZATION NAME(S) AND ADDRESS(ES)
University of New South Wales-NEW NCAGE Code
HIGH STREET
KENSINGTON, NSW
AU

8. PERFORMING ORGANIZATION REPORT NUMBER

9. SPONSORING/MONITORING AGENCY NAME(S) AND ADDRESS(ES)	10. SPONSOR/MONITOR'S ACRONYM(S)	11. SPONSOR/MONITOR'S REPORT NUMBER(S)
AOARD UNIT 45002 APO AP 96338-5002	AFRL/AFOSR IOA	AFRL-AFOSR-JP-TR-2024-0031

12. DISTRIBUTION/AVAILABILITY STATEMENT
A Distribution Unlimited: PB Public Release

13. SUPPLEMENTARY NOTES

14. ABSTRACT
While flying in outdoor conditions crafts will be required to not only perform robustly when encountering variations in ambient flows (gusts) but also be capable of producing rapid changes in aerodynamic forces during voluntary aerial maneuvers. Our knowledge of the receptivity of unsteady flow occurring over dynamically stalling wings to freestream-induced perturbations remains limited yet the likelihood of such interactions is high due to the iniquitousness of wind unsteadiness in the outdoor environment across all atmospheric regimes. This project focuses on the effects of pitch perturbations on a rotating wing by systematically varying the initial pitch angle, the amplitude of oscillations, and the duration of perturbation. The effects are analyzed by comparing the force coefficients and the flow structure over the wing. The power transfer from the fluid to the wing is also computed using the torque measurements. In chapter 2, we report on streamline penetration, velocity error and consequences of fluid-structure interaction solver based on the immersed boundary method and the lattice Boltzmann method (IB-LBM). This work contributes to a high-fidelity numerical framework developed to study the effects of freestream and kinematic perturbations on oscillating wings.

15. SUBJECT TERMS

16. SECURITY CLASSIFICATION OF:			17. LIMITATION OF ABSTRACT	18. NUMBER OF PAGES
a. REPORT	b. ABSTRACT	c. THIS PAGE		
U	U	U	SAR	49

19a. NAME OF RESPONSIBLE PERSON	19b. PHONE NUMBER *(Include area code)*
FUMIO KOJIMA	315-227-7007

Standard Form 298 (Rev.5/2020)
Prescribed by ANSI Std. Z39.18

The effects of freestream and kinematic perturbations on oscillating wings at low Reynolds numbers

Grant Number: FA2386-20-1-4084

Name and Position/Title of Principle Investigator:
Dr Sridhar Ravi, Associate Professor, UNSW-Canberra

Key Researcher(s) involved in the Proposed Project:
Dr Shantanu S. Bhat, Research Associate, UNSW-Canberra
Dr Qiuxiang Huang, Research Associate, UNSW-Canberra

Proposed Period of Performance: 30 Sep 20 - 29 Sep 22
Proposed Total Cost (for each year): 115.5k

Abstract

While flying in outdoor conditions crafts will be required to not only perform robustly when encoun-tering variations in ambient flows (gusts) but also be capable of producing rapid changes in aerodynamic forces during voluntary aerial manoeuvres. Our knowledge of the receptivity of unsteady flow occurring over dynamically stalling wings to freestream-induced perturbations remains limited yet the likelihood of such interactions is high due to the ubiquitousness of wind unsteadiness in the outdoor environment across all atmospheric regimes. This project focuses on the effects of pitch perturbations on a rotating wing by systematically varying the initial pitch angle, the amplitude of oscillations, and the duration of perturbation. The effects are analysed by comparing the force coefficients and the flow structure over the wing. The power transfer from the fluid to the wing is also computed using the torque measurements. In chapter 2, we report on streamline penetration, velocity error and consequences of fluid-structure interaction solver based on the immersed boundary method and the lattice Boltzmann method (IB-LBM). This work contributes to a high-fidelity numerical framework developed to study the effects of freestream and kinematic perturbations on oscillating wings.

Contents

1 Effects of pitch perturbations on a rotating wing at low Reynolds numbers 1
- 1.1 Introduction . . . 1
- 1.2 Methods . . . 2
  - 1.2.1 Experimental method . . . 2
  - 1.2.2 Numerical method . . . 4
  - 1.2.3 Quasi steady model predictions . . . 6
- 1.3 Results . . . 7
  - 1.3.1 Effect of the initial rest angle . . . 7
  - 1.3.2 Effect of the amplitude of perturbation . . . 9
  - 1.3.3 Effect of the duration of perturbation . . . 10
  - 1.3.4 Effect of pitch-axis location . . . 11
- 1.4 Discussion . . . 12
- 1.5 Conclusions . . . 16

2 Streamline penetration, velocity error and consequences of the feedback immersed boundary method 17
- 2.1 Introductions . . . 17
- 2.2 Numerical methods . . . 18
- 2.3 Fluid solver . . . 19
- 2.4 Structure solver . . . 20
- 2.5 Feedback immersed boundary method . . . 20
- 2.6 Results and Discussion . . . 23
  - 2.6.1 Flow over a cylinder . . . 23
  - 2.6.2 Flexible beam behind a stationary cylinder in a channel . . . 26
  - 2.6.3 Fluid flow through a 2-D asymmetric stenosis . . . 28
  - 2.6.4 One-sided collapsible channel flow . . . 31
  - 2.6.5 Three-dimensional collapsible tube flow . . . 33
  - 2.6.6 Discussions . . . 35
- 2.7 Conclusions . . . 37

3 Performance Metric 46
- 3.1 Peer-reviewed Journal and Conference Papers . . . 46

1 Effects of pitch perturbations on a rotating wing at low Reynolds numbers

1.1 Introduction

Fluid dynamics of rotating wings are of high interest to engineers for their applications in turbomachines, rotorcrafts, and micro-air vehicles. The geometry of a rotating wing can be broadly defined by the ratio of the wingspan (b) to the mean wing chord ($\bar{c}$), also known as the aspect ratio ($AR = b/\bar{c}$). The kinematics of the wing depends on its Reynolds number ($Re = U_{ref}\bar{c}/\nu$), where U_{ref} is the reference velocity, typically at the radius of gyration of the wing, and ν is the kinematic viscosity of the fluid around the wing. Motivated by the aerodynamics of winged seeds and insect wings at low Reynolds numbers ($Re < 10^5$), the small aspect-ratio wings ($AR < 5$) have been investigated for their possible small-size engineering applications (e.g. Ennos, 1989; Lentink et al., 2009; Kruyt et al., 2015).

At such low Reynolds numbers, the flow over the wing separates at its leading edge, forming a leading-edge vortex (LEV) over the wing's suction surface (Ellington et al., 1996). Due to the spanwise gradient of the flow during the wing's rotation (sweep motion), the LEV also varies in size along the span, making it to be smaller near the wing root and larger towards the wing tip. For a wing held at a constant angle (α) and rotating with a constant angular velocity ($\dot{\phi}$), the LEV is stabilised in its place and size by the action of the strong centripetal and Coriolis accelerations (Lentink and Dickinson, 2009; Jardin, 2017). The stably attached LEV creates a stable suction pressure on the wing surface beneath the LEV. Consequently, the forces on the rotating wing are also found to be stable (Dickinson et al., 1999; Birch et al., 2004). However, a change in the wing's angle due to the wing's rotation about its spanwise axis (pitch motion) may disturb the stability of the LEV, affecting the wing performance. Such disturbance may arise in the case, for example, of pitching-flapping perturbed revolving wings employed in micro-air vehicles (Chen et al., 2020a) or during the pitch-oscillations in the flapping motion of wings (Sum Wu et al., 2019). However, the effects of such pitch perturbations on the flow and the forces on the wing remain under-explored.

Many researchers in the past have explored the pitch perturbations on linearly translating wings (e.g. McCroskey, 1982; Walker et al., 1985; Acharya and Metwally, 1992; Ol et al., 2010). Such perturbations have been reported to cause dynamic stall on the translating wings (McCroskey, 1982). This is because the instantaneous lift on oscillating wings differs from its static values at the same angles of attack and follows a different trend during the pitch-up and pitch-down motions, resulting in a hysteresis loop (Corke and Thomas, 2015). At high angles of attack, the shear layer separated from the leading edge has been observed to oscillate with a phase difference with the wing's pitch oscillations (Bhat and Govardhan, 2013; Menon and Mittal, 2019). The forces acting on the wing vary in magnitude dependent on the strength and phase of the shear-layer oscillations. In fact, some low-frequency pitch oscillations can draw power from the fluid resulting in self-excitation or flutter. However, this does not explain the pitch-perturbation effects on rotating wings because the mechanism of a stable LEV is absent in the linearly translating wings. Moreover, rotating wings at low Reynolds numbers do not experience static stall due to the stable LEV. Hence, a possibility of dynamic stall in rotating wings needs to be examined.

Recently, Chen et al. (2018, 2020a) have reported the dynamic behaviour of forces acting on a rotating wing at $Re = 1500$ during its pitch and flapping perturbations. However, it

should be noted that their initial angle of attack (α_0) was chosen to be 0° and 20°, while most studies on rotating and flapping wings use much higher angles $\alpha_0 \sim 45°$. The lift and drag on rotating wings depend highly on α (Sane and Dickinson, 2001). Investigating wider ranges of α_0 and pitching amplitudes ($\Delta\alpha$) is necessary to improve our understanding of the LEV and its dynamics applicable to a larger number of studies.

Hence, the present study focuses on the effects of pitch perturbations on a rotating wing by systematically varying the initial pitch angle (α_0), the amplitude of oscillations ($\Delta\alpha$), and the duration of perturbation (T_p). The effects are analysed by comparing the force coefficients and the flow structure over the wing. The power transfer from the fluid to the wing is also computed using the torque measurements.

1.2 Methods

This investigation required the measurement of forces and torques to analyse the wing performance and the measurement of wing surface pressure and flow field data to analyse the effects of flow around the wing on the wing performance. The forces and torques were measured experimentally, which allowed for gathering data for a wide parameter space. The pressure and flow-field data were predicted for a few chosen cases of interest using computational fluid dynamics (CFD) simulations. Both methods are described below in detail.

1.2.1 Experimental method

Experiments were conducted on a rectangular wing of span $b = 150$ mm and chord $c = 50$ mm placed at the centre of a water tank of size $900 \times 900 \times 600$ mm^3. This size was large enough to have minimal effects from sidewalls (Karakas and Fenercioglu, 2016). The schematic of the experimental setup is shown in figure 1(a). The wing was cut from a 1-mm thick aluminium sheet and was provided with a root cutout of 35×21 mm^2 to accommodate a force/torque sensor (ATI Nano17 IP68 F/T sensor) at its root, as shown in figure 1. The wing along with the sensor was attached to a timing pulley near the bottom of the main shaft of a flapping mechanism, driven by a timing belt and another pulley at the top. The motion of the main shaft about the flapping (Y) axis and that of the timing pulley about the pitching (Z) axis was provided by two identical RoboStar SBRS-5314HTG servo motors, as described by Mazharmanesh et al. (2021). Due to the pulley and the attachments, the wing root was offset from the axis of rotation by $b_0 = 20$ mm. The normalised offset $b_0/b = 0.13$ was within the range of having a negligible effect on the LEV over the wing (Bhat et al., 2018).

The wing was initially held at rest at a constant angle of attack α_0 and was then rotated about the Y axis with the Reynolds number of $Re = \rho U_{ref} c/\mu = 2500$, where the reference velocity is $U_{ref} = 0.75R\dot{\phi}$, R is the wing-tip radius with respect to the flapping axis ($R = b+b_0$), $\dot{\phi}$ is the constant rotational velocity of the wing and $\rho = 1000$ kg/m^3 and $\mu = 8.9 \times 10^{-4}$ Pa-s are respectively the density and viscosity values of the water in the tank. In each experiment, the wing was rotated by 160 degrees and retracted to the initial position, followed by a rest period of 2 minutes to allow the disturbed water to settle back to its near-quiescent state. During the flapping stroke at a constant $\dot{\phi}$, the wing's angle of attack was perturbed by the amplitude $\Delta\alpha$ after time $t_1 = 0.4T$ using a constant pitch angular velocity until $t_2 = t_1 + T_p/2$ and was returned to the original angle α_0 by $t_3 = t_1 + T_p$.

The forces and torques acting on the wing were measured by the ATI Nano17 IP68 F/T sensor at the sampling rate of 1000 Hz using a National Instruments PCI-6143 DAQ board

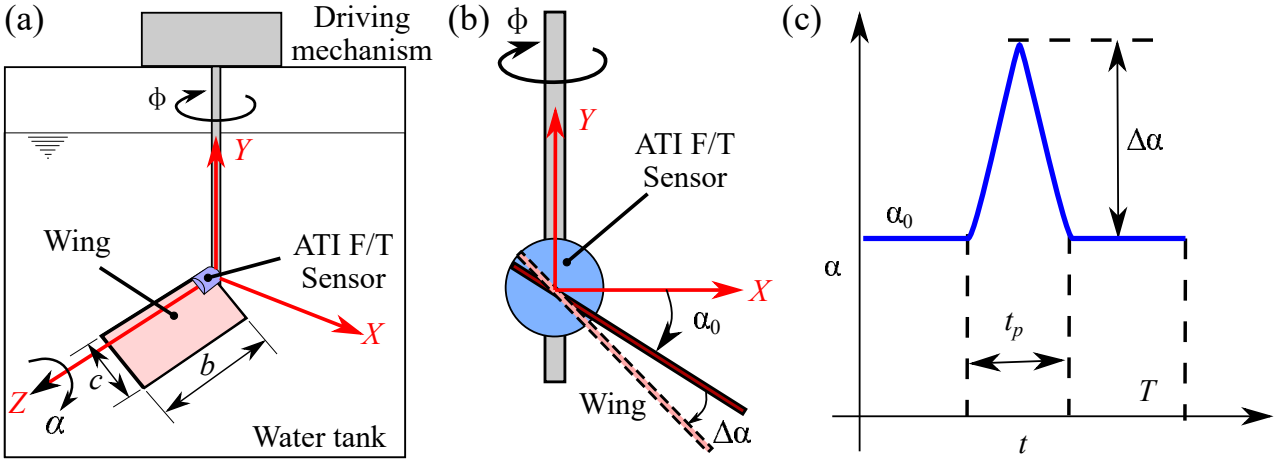

Figure 1: The schematic shows (a) the rotating wing experimental setup in a water tank, (b) the front view of the wing showing its initial angle α_0 and the magnitude of perturbation $\Delta\alpha$, and (c) typical target time traces of the wing angle α, also showing the time period of the perturbation T_p and the time period of the rotational stroke T.

linked to a PC. With the SI-50-0.5 calibration, the ATI sensor was capable of measuring forces in three dimensions with an accuracy of 12.5 mN and torques in three dimensions with an accuracy of 0.0625 Nmm. The servo motors' potentiometer signals were recorded to estimate the wing's actual angular positions simultaneously with the force data. The total duration of an experiment included recording the forces and torques during the first 3 s of rest before the start, 9 s of wing rotation, and 3 s of rest after stopping the wing. Each experiment was repeated 5 times and the filtered data were found to be highly repeatable within the margin of 3% for the largest pitch perturbation of the chosen parameter space.

The recorded raw data were processed using an in-house Python code. The raw data were filtered at the cutoff frequency of $f_c = 4/t_p$ using a fourth-order Butterworth filter. The recorded forces were the sum of the fluid-mechanical forces, weights, inertial forces and added-mass forces. The inertial forces were identified by repeating the experiments in air and subtracting the weight in the air, since the fluid-mechanical and added mass forces are negligible in air. According to the expressions given by Lee et al. (2016), the added-mass force and torque were estimated using

$$\begin{aligned} F_{am} &= f_a \rho \frac{\pi}{4}\left[\ddot{\phi}\sin\alpha\int_0^R c(r)^2 r\mathrm{d}r + \ddot{\alpha}\int_0^R c(r)^2\left(\frac{c(r)}{2} - x_{rot}\right)\mathrm{d}r\right], \qquad \text{and} \\ \tau_{am} &= -f_t \rho \frac{\pi}{128}\ddot{\alpha}\int_0^R c(r)^4\mathrm{d}r, \end{aligned} \tag{1}$$

respectively, where $f_a = 0.773 + 1.903Re^{-0.687}$ and $f_t = 1.056 + 7.49Re^{-0.855}$ are the correction factors, $c(r)$ is the local chord length at a spanwise distance r, ϕ is the sweep-angular displacement and α is the pitch-angular displacement. The inertial and added mass effects were subtracted from the measured data to obtain the fluid-mechanical forces. These forces were used to compute the lift and drag forces acting along the Y and X directions, respectively, in the rotating frame of reference, as shown in figure 1(b). the lift and drag coefficients are defined as

$$C_L = \frac{2L}{\rho U_{ref}^2 S} \quad \text{and} \quad C_D = \frac{2D}{\rho U_{ref}^2 S}, \tag{2}$$

where S is the wing area.

The initial rest angle and target perturbation amplitude were both systematically varied in the range $[0° - 90°]$ in the steps of 15°. Both pitch-up and pitch-down perturbations were investigated. Two different values of the normalised duration of perturbation $\tau = T_p/T = 0.2$ and 0.4 were chosen to understand its effect on the wing performance. Note that the actual recorded values of $\Delta\alpha$ with $\tau = 0.2$ were found to be, approximately, in the multiples of 13° and those with $\tau = 0.4$ were found to be, approximately, in the multiples of 14.5° due to the limitation of the motor's acceleration to quickly reach the target constant pitch speed, as can be seen in figure 2.

1.2.2 Numerical method

The numerical method used here has been adopted from that of Harbig et al. (2013) and Bhat et al. (2019a), which has been validated for rotating and flapping wings in the range of the Reynolds numbers $150 \leq Re \leq 4000$. Flow over the wing was simulated by directly solving Navier-Stokes equations in a non-inertial rotating frame of reference using the commercial code Ansys CFX 21.1.

In this method, a rectangular wing, offset from the rotation axis similar to that in experiments, was located at the centre of a cylindrical domain of diameter $18R$ and height $48c$. The rotation axis of the wing was aligned with the axis of the cylinder. The domain was split into the outer 'rotary' subdomain and the inner 'pitching' subdomain. The inner spherical pitching subdomain of diameter $2.4R$ was situated at the centre of the cylindrical domain. The entire domain was discretised using an unstructured tetrahedral mesh with triangular prism elements near the wing surface. The overall mesh consisted of approximately 8 million elements, with a grid spacing of $0.0145c$ on the wing surface. Following the recommendations of Harbig et al. (2013), the time step of $T/(2\phi_A)$ was used, where T is the total duration of the rotational stroke and ϕ_A is the total rotation amplitude in degrees. The grid convergence was ensured by repeating the case with $\alpha_0 = 15°$, $\Delta\alpha = 60°$ and $\tau = 0.2$, using coarse, medium, and fine grids obtained by changing the grid spacing by the factor of 2 in each refinement. Both instantaneous and mean variations in C_L and C_D were observed to be within 1% between the medium and fine grids.

The top and bottom faces of the cylinder were modelled as openings. The cylindrical surface was modelled as a free-slip wall. The wing surfaces were modelled as no-slip walls. The mesh in the inner spherical subdomain was fixed with respect to the wing and was allowed to rotate about the wing's pitching axis with the angular velocity $\dot{\alpha}$ using the 'Mesh Motion' tool in Ansys CFX. A general grid interface (GGI) connection was applied at the interface between the two non-conformal subdomains.

The wing was initially set to be at rest at an angle α_0 with the horizontal plane. It was then accelerated within the first 0.5 s to the rotational velocity $\dot{\phi} = 20$ deg/s and was then rotated with a constant rotational velocity until $t = 8.5$ s, followed by a deceleration to $\dot{\phi} = 0$ deg/s within the final 0.5 s. The pitch angle α underwent one perturbation $\Delta\alpha$ during this motion, the same as that described in the experimental method. As mentioned earlier, the actual variation in α in experiments was observed to be different from the target profile. Hence, the variation in α in the numerical simulations was specified using the cosh function with its smoothing coefficient and amplitude modified to closely match the experimental data of α, as can be seen in figure 2.

Two cases were simulated for validating the numerical method; first, with $\Delta\alpha = 13°$ and

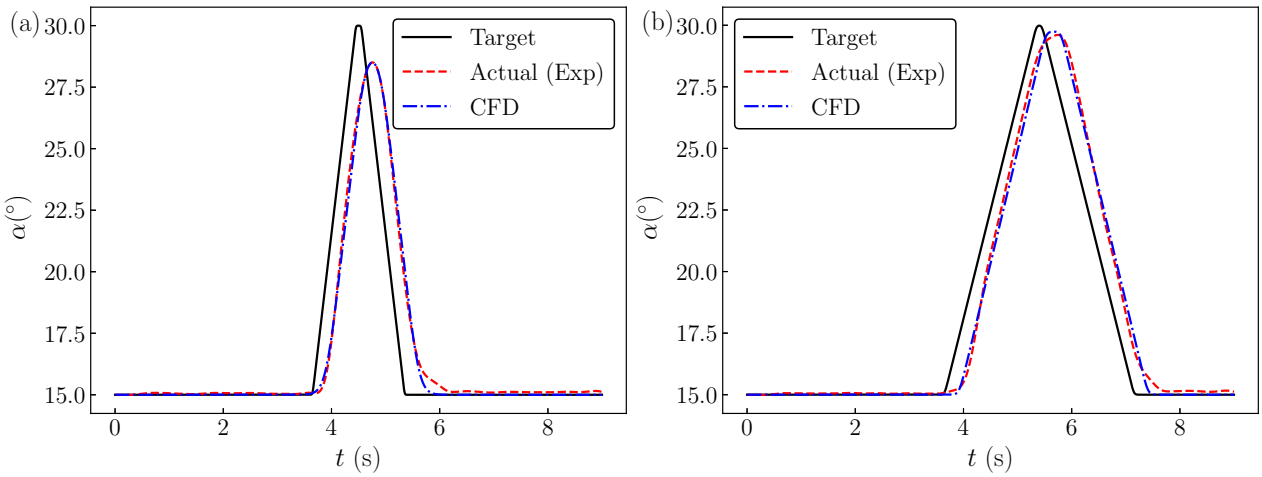

Figure 2: The target time traces of α are compared with those obtained in experiments and the closely matching profile provided in CFD. Here, $\alpha_0 = 15^\circ$, target $\Delta\alpha = 15^\circ$, and the normalised target duration of perturbation $\tau = 0.2$ in (a) and $\tau = 0.4$ in (b).

second, with $\Delta\alpha = 52^\circ$, as shown in figure 3(a). In both cases, $\alpha_0 = 15^\circ$ and $\tau = 0.2$ were chosen to be the same. Figures 3(b) and (c) show the time traces of C_L and C_D predicted by CFD. For both cases, the time traces of C_L match the experimental data better than the time traces of C_D do. Since the difference between the experimental and CFD results was within the range of the uncertainty in experimental measurements, a quasi-steady model of Lee et al. (2016) was used to predict C_L and C_D. The quasi-steady model estimates showed a very close match with the CFD predictions, confirming the results. The model is described in detail in the following section.

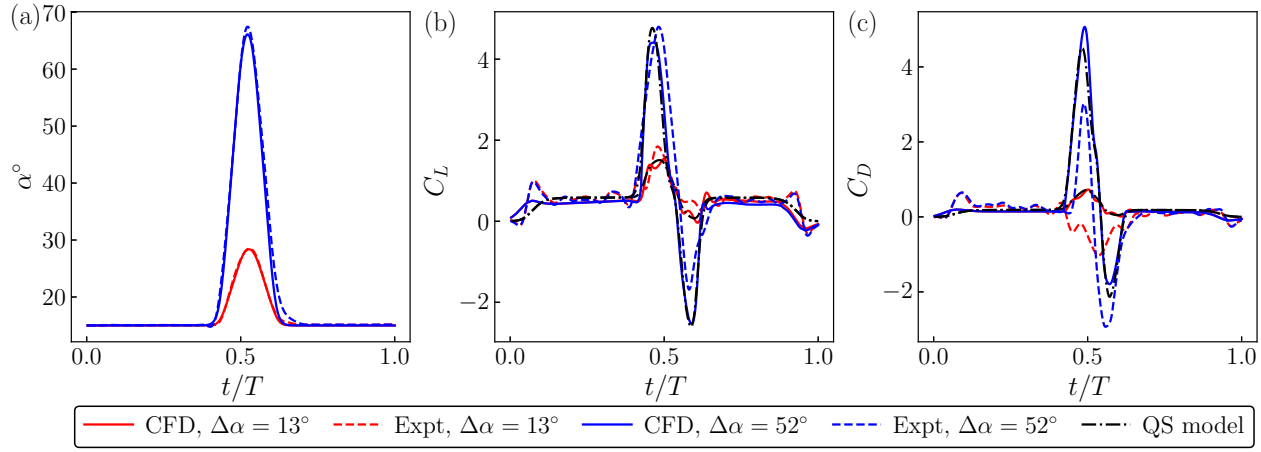

Figure 3: Time traces of (a) α, (b) C_L and (c) C_D are shown for two different perturbation amplitudes, $\Delta\alpha = 13^\circ$ and 52°. In both cases, $\alpha_0 = 15^\circ$ and $\tau = 0.2$. The CFD predictions are compared with the experimental data and the quasi-steady model predictions (Lee et al., 2016).

1.2.3 Quasi steady model predictions

Several quasi-steady models have been developed, for example by Sane and Dickinson (2002), Truong et al. (2011), Han et al. (2015), and Lee et al. (2016), predicting forces and torques on rotating and flapping wings. The quasi-steady model proposed by Lee et al. (2016) takes into account the effects due to the wing's Reynolds number, aspect ratio, and Rossby number, which are important parameters having coupled effects on the wing performance (Bhat et al., 2019b). The model of Lee et al. (2016) has been employed for more accurate predictions of forces on the pitch-perturbed rotating wing. This also provided insights into the force generation mechanism by decomposing the forces into various components.

According to this model, the lift (L) and drag (D) forces on a wing can be decomposed as

$$L = L_{tr} + (F_{rot,1} + F_{rot,2} + F_a)\cos\alpha \quad \text{and} \quad D = D_{tr} + (F_{rot,1} + F_{rot,2} + F_a)\sin\alpha, \tag{3}$$

respectively. Here, L_{tr} and D_{tr} are the lift and drag components due to the wing's rotational translation, i.e. the stroke motion, $F_{rot,1}$ and $F_{rot,2}$ are the forces due to the wing's rotation about the pitch axis, F_a is the force due to the added mass and α is the wing's angle of attack. The translational components are given by

$$\begin{aligned} L_{tr} &= f_{AR,tr} f_{Ro,tr} C_{L,tr} \left(0.5\rho\dot{\phi}^2 \int_0^R cr^2 dr\right) \qquad \text{and} \\ D_{tr} &= f_{AR,tr} f_{Ro,tr} C_{D,tr} \left(0.5\rho\dot{\phi}^2 \int_0^R cr^2 dr\right), \end{aligned} \tag{4}$$

where $f_{AR,tr}$ is the aspect ratio correction factor:

$$f_{AR,tr} = 32.9 - 32AR^{-0.00361} \tag{5}$$

and $f_{Ro,tr}$ is the Rossby number correction factor:

$$f_{Ro,tr} = -0.205\tan^{-1}[0.587(Ro - 3.105)] + 0.87. \tag{6}$$

The translational lift and drag coefficients are dependent on the Reynolds number (Re) and α and are given by

$$\begin{aligned} C_{L,tr} &= (1.966 - 3.94Re^{-0.429})\sin(2\alpha) \qquad \text{and} \\ C_{D,tr} &= (0.031 + 10.48Re^{-0.764}) + (1.873 - 3.14Re^{-0.369})[1 - \cos(2\alpha)], \end{aligned} \tag{7}$$

respectively. The rotational force $F_{rot,1}$ is due to the circulation around the wing as a result of pitch rotation, as per the conventional Kutta-Joukowski theory and can be predicted by:

$$F_{rot,1} = f_\alpha f_r (0.927 - 0.558Re^{-0.1577})\dot{\phi}\dot{\alpha}\int_0^R c^2 r dr. \tag{8}$$

Here, f_α is the factor dependent on the instantaneous α as

$$f_\alpha = \begin{cases} 1 & -45^\circ < \alpha < 45^\circ \\ -1 & 135^\circ < \alpha < 225^\circ \\ \sqrt{2}\cos\alpha & \text{otherwise.} \end{cases} \tag{9}$$

Moreover, f_r is the factor due to the location of the wing's pitching axis with respect to the leading edge (x_{rot}) as

$$f_r = 1.57 - 1.239\left(\frac{1}{R\overline{c}}\int_0^R x_{rot}dr\right). \tag{10}$$

Similarly, the force $F_{rot,2}$ is due to the local drag force acting on the wing as a result of the wing's instantaneous pitch rotation and is given by

$$F_{rot,2} = 2.67\rho\dot{\alpha}|\dot{\alpha}|\int_{LE}^{TE} rx|x|dx, \tag{11}$$

where x is the chordwise distance measured from the pitch axis and is positive in the direction towards the trailing edge (TE). The forces due to added mass were calculated as per equation 1. The decomposition of forces using the quasi-steady (QS) model was used to analyse various effects, as discussed later in the results.

1.3 Results

1.3.1 Effect of the initial rest angle

For a rotationally translating wing without a pitch perturbation, the values of C_L and C_D are directly related to the rest α_0, which would remain constant throughout the rotation of the wing. However, the pitch perturbation changes the instantaneous α, which would disturb C_L and C_D. This was analysed by studying the effect of α_0 on the wing performance. Keeping $\Delta\alpha = 52°$ and $\tau = 0.2$, α_0 was varied in the steps of 15°. Figure 4 shows that both C_L and C_D were affected by α_0.

As expected, both C_L and C_D initially increased when the wing was accelerated from rest, and they reached nearly stable values close to $t/T = 0.2$. From this point until the start of the pitch perturbation, the wing was in the pure rotational translation, as shown by the shaded region in the figure. The corresponding values of C_L and C_D in this region are denoted by $C_{L,tr}$ and $C_{D,tr}$, respectively. As per the quasi-steady model proposed by Lee et al. (2016), $C_{L,tr} \propto \sin(2\alpha)$ and $C_{D,tr} \propto 1 - \cos(2\alpha)$. The averaged values in this region (i.e. $\overline{C}_{L,tr}$ and $\overline{C}_{D,tr}$) appear to follow the same trend, as shown in figure 5(a).

The values of both C_L and C_D varied during the pitch perturbation and returned to the values close to their original values after the perturbation was stopped. The peak-to-peak variations in C_L and C_D, i.e. ΔC_L and ΔC_D, respectively, changed depending on the initial angle α_0 even when the perturbation magnitude $\Delta\alpha$ was kept constant. The maximum variation in C_L was observed for $\alpha_0 = 0°$, which reduced with an increase in α_0. This can be explained by the contribution of the normal force $F_{n,rot} = F_{rot,1} + F_{rot,2}$ to the lift and drag at different wing angles. The force $F_{n,rot}$ is proportional to the pitch angular velocity $\dot{\alpha}$ and will act in the direction normal to the wing surface. The contribution $F_{n,rot}$ to the lift can be given by $F_n \cos\alpha$ and that to the drag can be given by $F_n \sin\alpha$. Its effect on ΔC_L and ΔC_D can be analysed against the mean perturbation angle, defined by

$$\overline{\alpha}_p = \frac{1}{T_p}\int_{t_1}^{t_1+T_p} \alpha\, dt. \tag{12}$$

The peak-to-peak variation in $F_{n,rot}$ must be the same across all the cases due to the same $\dot{\alpha}$ profiles. However, its contribution to the lift is expected to reduce with $\overline{\alpha}_p$ and that with drag is expected to increase with $\overline{\alpha}_p$, as has been confirmed by the observations in figure 5(b).

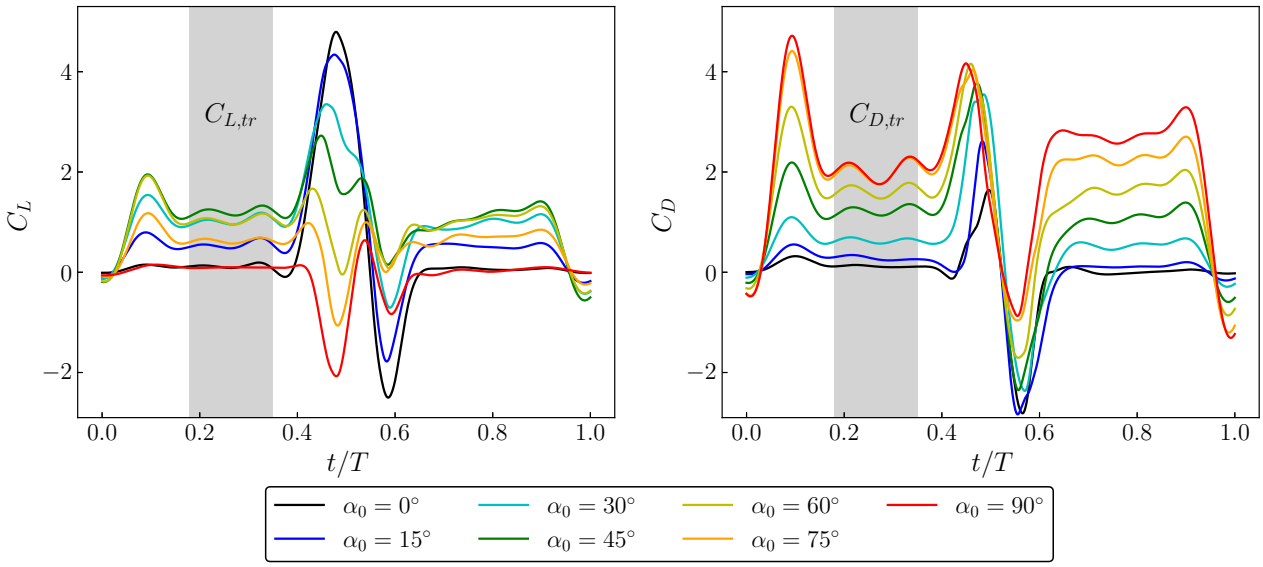

Figure 4: Time traces of (a) C_L and (b) C_D are shown for various α_0. Across all the cases compared here, $\Delta\alpha = 52°$ and $\tau = 0.2$.

Furthermore, the rotational force $F_{n,rot}$ itself can be changed by changing the $\dot{\alpha}$ profile. This can be achieved either by perturbing the pitch with a different magnitude in the same time period T_p or by changing the time period T_p for a given perturbation magnitude. Both of these are explored in the following subsections.

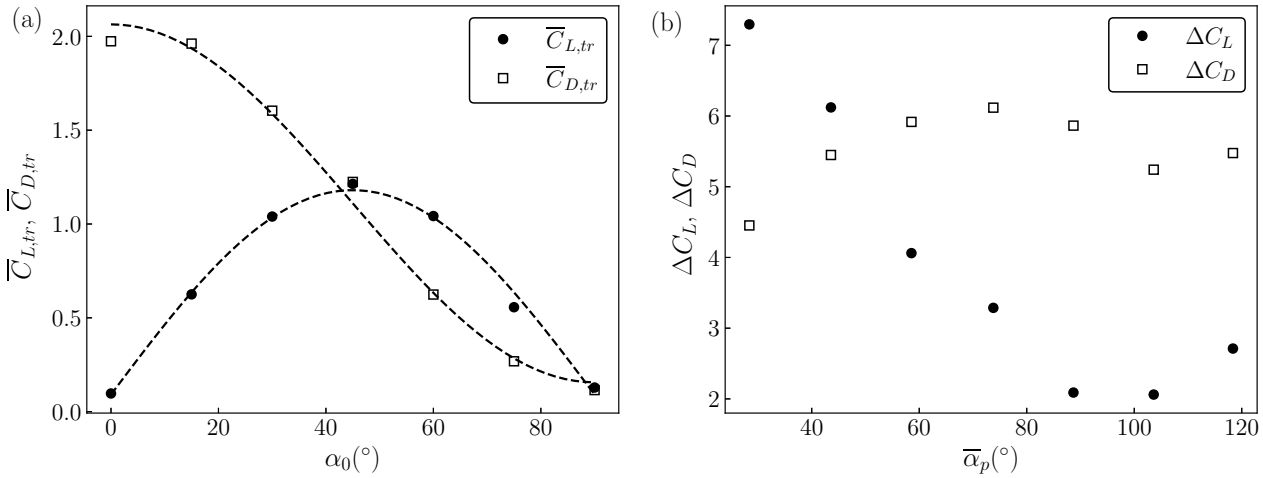

Figure 5: The time-averaged $C_{L,tr}$ and $C_{D,tr}$ during the pure translational motion are shown as functions of α_0 in (a). The dashed lines show the fit to $\sin(2\alpha_0)$ for the $\overline{C}_{L,tr}$ data and to $[1-\cos(2\alpha_0)]$ for the $\overline{C}_{D,tr}$ data. The peak-to-peak variations ΔC_L and ΔC_D during the pitch perturbation are shown as functions of the mean pitch perturbation angle $\overline{\alpha}_p$ in (b). Here, in all cases, $\Delta\alpha = 52°$ and $\tau = 0.2$.

1.3.2 Effect of the amplitude of perturbation

The amplitude of perturbation $\Delta\alpha$ was systematically varied to observe the effects on C_L and C_D, as shown in figure 6. The initial rest angle ($\alpha_0 = 15°$) and the duration of perturbation ($\tau = 0.2$) were kept constant across all cases. Here, both, pitch-up and pitch-down perturbations were examined by varying the target $\Delta\alpha$ in the steps of 15°. Due to the limitations in the acceleration of the servomotors, the resulting $\Delta\alpha$ in the actual experiment was varied in the steps of $\sim 13°$. During the pitch-up perturbations, C_L was observed to rise and fall during the first half of the perturbation. During the remaining half, C_L decreased to lower values than $C_{L,tr}$ and returned to the original value at the end of perturbation. On the other hand, during the pitch-down perturbations, the waveform of C_L was observed to be inverted. Moreover, the peak-to-peak variations in C_L were directly proportional to $\Delta\alpha$ in both pitch-up and pitch-down perturbations. This can be attributed to the fact that during the same τ, achieving a higher $\Delta\alpha$ would require a higher $\dot{\alpha}$ and this will increase the force component $F_{n,rot}$. During the pitch-down perturbations, the value of $\dot{\alpha}$ is reversed, causing $F_{n,rot}$ also to change its direction.

C_D was also observed to vary in similar ways as C_L in pitch-up perturbations, having an increased magnitude with a larger $\Delta\alpha$. However, in the pitch-down perturbations, the waveform of C_D was not inverted. This is because the initial angle, α_0 chosen here, itself is very small, due to which the direction of $F_{n,rot}$ would always be inclined in the direction of the flow during the first half of the perturbation, irrespective of the sign of $\dot{\alpha}$. Thus, its component contributing to the drag would be positive during this time. Furthermore, the results show that in all cases, C_L and C_D returned to their initial values immediately after the perturbation was stopped. Thus, the change in the flow structure over the wing due to the perturbations appears to have less influence on C_L and C_D, which will be analysed later in detail.

Pitch perturbations in a linearly translating wing are known to result in the phenomenon of the dynamic stall, which introduces a hysteresis in the variation in C_L as a function of α. The

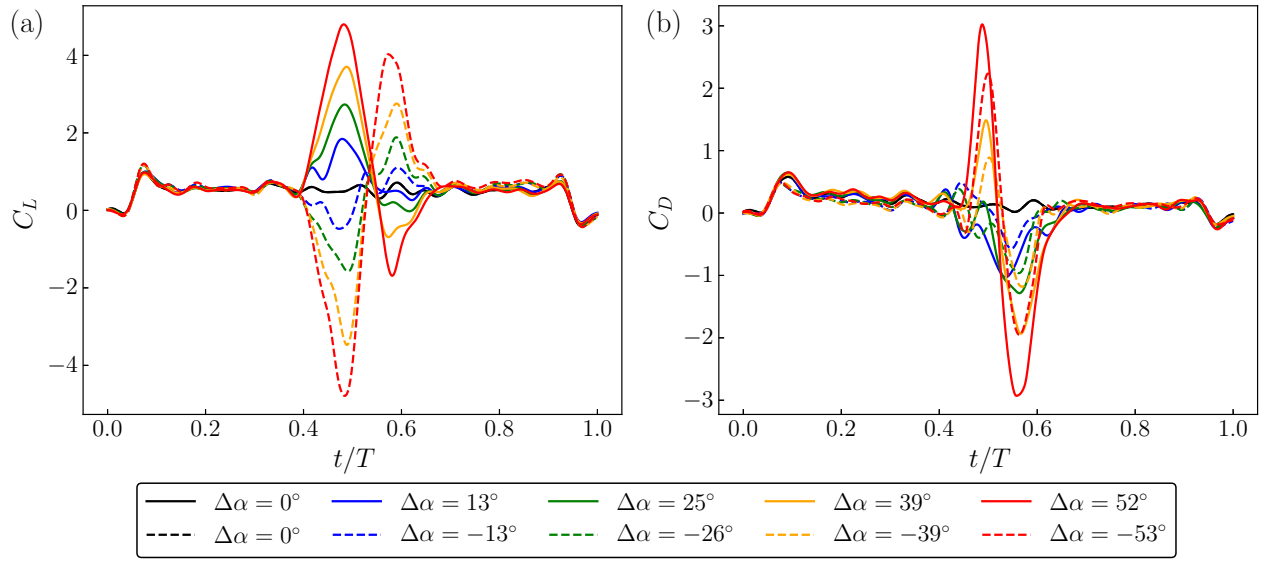

Figure 6: The time traces of (a) C_L and (b) C_D are shown for various $\Delta\alpha$. The solid lines represent the pitch-up perturbations while the dashed lines represent the pitch-down perturbations.

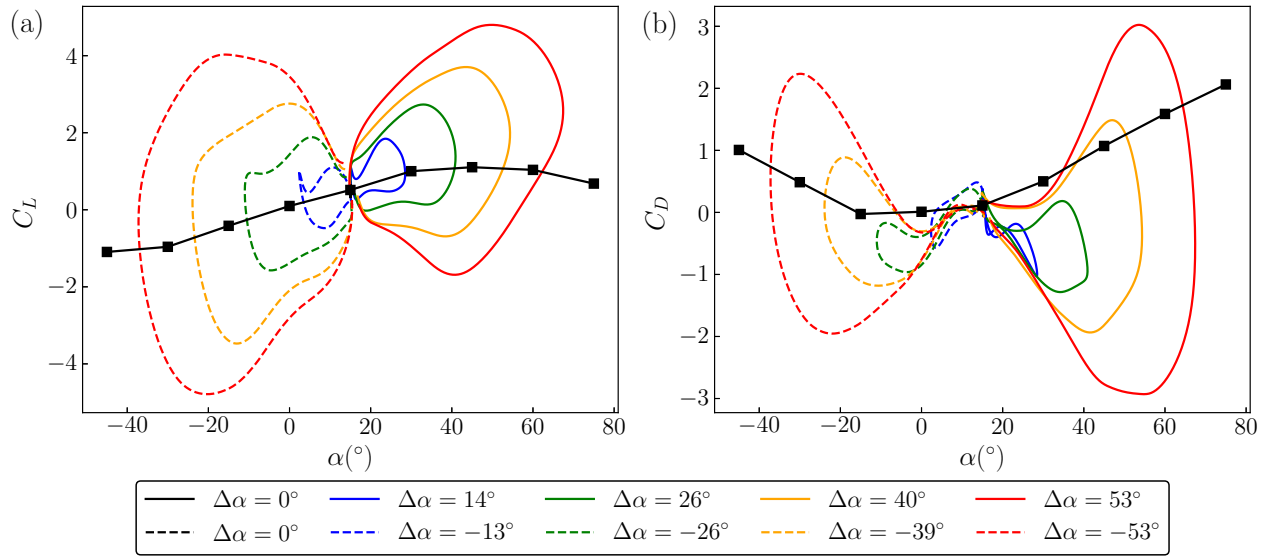

Figure 7: Instantaneous values of (a) C_L and (b) C_D are plotted against the instantaneous α, showing the hysteresis during the pitch perturbations. The black lines represent the data without any pitch perturbations. In these cases, $\Delta\alpha$ is varied while maintaining $\alpha_0 = 15^\circ$ and $\tau = 0.2$.

same effect was also investigated in the case of a rotationally translating wing in the present work, as shown in figure 7. Here, the data for the instantaneous C_L and C_D from figure 6 have been plotted as a function of the instantaneous α. The black lines in figures 7(a) and (b) represent the stabilised C_L and C_D values as functions of α for an unperturbed pitch. Note that, unlike the linearly translating wings, the rotating wings do not follow the $C_L = 2\pi\alpha$ curve, since C_L due to the rotational translation is proportional to $\sin(2\alpha)$. Nevertheless, even in the case of rotating wings, the pitch perturbations were observed to introduce hysteresis in C_L around the curve showing the static-pitch data. The size of the hysteresis loop increased with $\Delta\alpha$ due to the increased pitch-rotational velocity effects.

As can be seen in figure 7(b), C_D also shows a variation around the static-pitch curve. The values of C_D with perturbations are mostly lower than the static values. However, it should be noted that the average C_D in all cases is in the range ($-1 \leq \overline{C}_D \leq 1$), which is within the experimental uncertainty. Hence, a more careful investigation is required to accurately determine the possibility of reducing drag using pitch perturbations.

1.3.3 Effect of the duration of perturbation

The pitch-rotation effects can also be changed by varying the duration of perturbation T_p. To investigate those effects, two values of the normalised duration of perturbation were compared, i. e. $\tau = 0.2$ and 0.4, as can be seen in figure 8. For a chosen amplitude of perturbation $\Delta\alpha$, the hysteresis loop obtained for $\tau = 0.4$ is observed to be smaller than that for $\tau = 0.2$. This is because, for the same amplitude, the larger duration would require a lower $\dot{\alpha}$. This would result in lower rotational effects in terms of the values of $F_{rot,1}$ and $F_{rot,2}$, as discussed earlier. In this figure, for a similar target $\Delta\alpha$, the actual $\Delta\alpha$ achieved is slightly different for $\tau = 0.2$ and 0.4 due to the difference in the servo motor's acceleration in the two cases. With a lower pitch acceleration with $\tau = 0.4$, the wing was able to reach $\Delta\alpha$ closer to the target value.

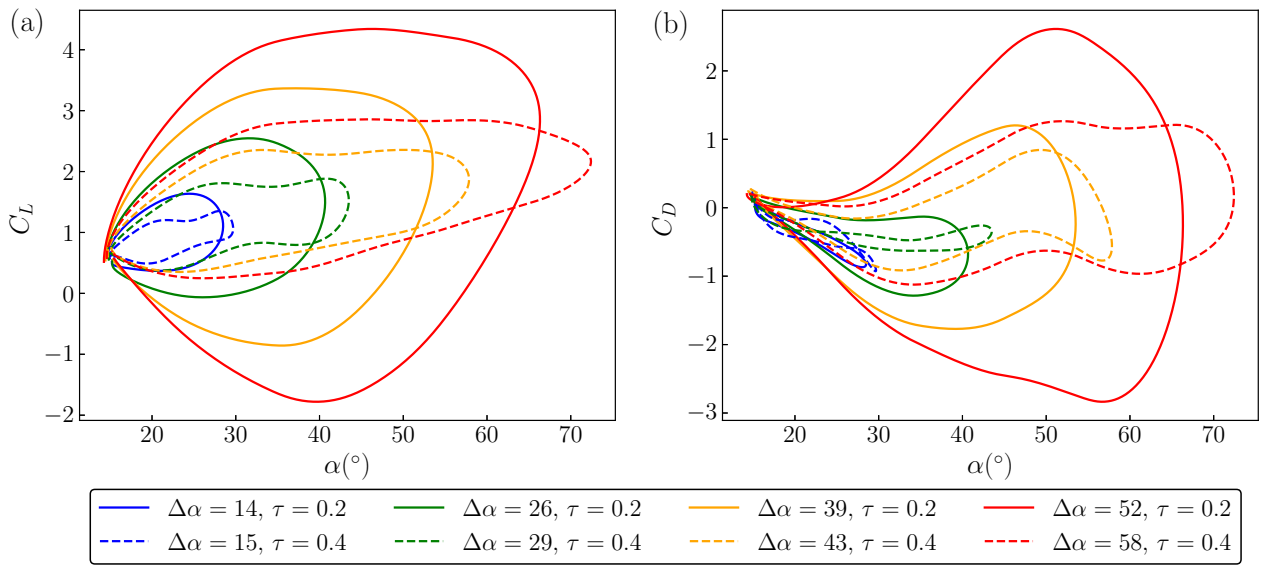

Figure 8: Instantaneous values of (a) C_L and (b) C_D are plotted against the instantaneous α for various $\Delta\alpha$. Here, solid lines represent $\tau = 0.2$ and dashed lines represent $\tau = 0.4$. In all cases, $\alpha_0 = 15°$.

Nevertheless, the lower values of $\dot{\alpha}$ resulted in lower hysteresis effects, as is evident from the figure.

Overall, hysteresis does appear in the pitch-perturbed rotating wing, similar to that observed in the pitch-perturbed linearly translating wings. In the case of rotating wings, the hysteresis is due to the effects of the pitch-rotation velocity. Thus, a smaller amplitude of perturbation during the same duration or a larger duration for the same amplitude would both reduce the hysteresis effects.

1.3.4 Effect of pitch-axis location

The force due to the rotational effects, which are responsible for the high variations in C_L and C_D, has two parts, namely, $F_{rot,1}$ and $F_{rot,2}$, as described earlier in eqs. (8) to (11). The second part, $F_{rot,2}$, depends on the integral $\int_{LE}^{TE} rx|x|dx$, where x is measured from the pitch axis in the chordwise direction. Thus, the value of $F_{rot,2}$ is directly dependent on the pitch-axis location. Its value will be 0 if the pitch axis is located at the centre of the wing chord. Consequently, the pitch axis location might affect the overall wing performance. These effects were analysed by numerically simulating two cases, one with the pitch axis located at the normalised location $\hat{x}_{pa} = x_{pa}/c = 0.2$ and the other with the pitch axis located at $\hat{x}_{pa} = 0.5$. The values $\alpha_0 = 15°$, $\Delta\alpha = 52°$, and $\tau = 0.2$ were maintained to be the same in both cases. The time traces of C_L and C_D for the two cases are shown in figure 9.

In this figure, the predictions of CFD match well with the quasi-steady model estimates. The net C_L and C_D are decomposed into the translational effects (trans), rotation effects estimated by the Kutta-Joukowski theory (rot1), and rotational effects from the local drag force normal to the wing surface (rot2). Since the translation effects are independent of the pitch axis location, the resulting time traces of the translational force coefficients are the same in both cases. However, the component rot2 is 0 in the case with $\hat{c}_{pa} = 0.5$, as

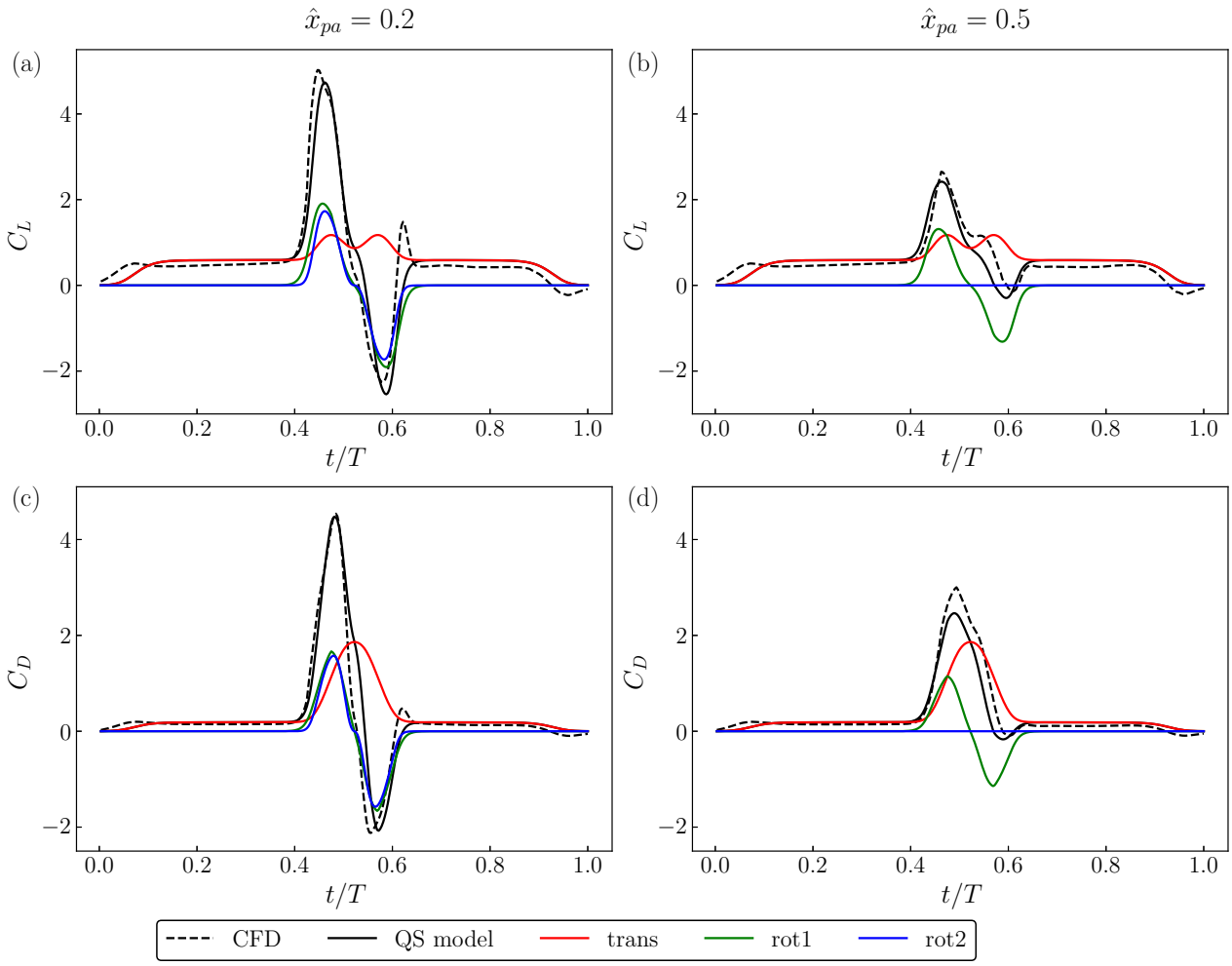

Figure 9: Figures (a) and (c) show the time traces of C_L and C_D, respectively, with the normalised chordwise location of the pitch axis $\hat{x}_{pa} = 0.2$, whereas (b) and (d) show the same time traces with $\hat{x}_{pa} = 0.5$. The dashed lines represent the CFD results while the solid lines represent the quasi-steady model estimations. Here, the force coefficients have been decomposed into the ''tr', i.e. translational effects (red), 'rot1', i.e. the pitch-rotational effect as per the conventional Kutta-Joukowsky theory (green) and 'rot2', i.e. the pitch-rotational effects giving rise to the local drag forces (blue). In both cases, $\alpha_0 = 15°$, $\Delta\alpha = 60°$, and $\tau = 0.2$.

predicted. Therefore, the variations in the net values of C_L and C_D are reduced. Note that both rotational components $F_{rot,1}$ and $F_{rot,2}$ depend on $\dot{\alpha}$. Hence, their mean value is 0. As a result, the average values of C_L and C_D only depend on the average of the translational components. Thus, the change in the pitch-axis location does not affect the average wing performance.

1.4 Discussion

To analyse the effects of the flow structures around the wing on the wing performance during the pitch perturbation, the normalised wing-surface pressure [$p^* = p/(0.5\rho U ref^2)$] contours

were plotted at various time steps along with the flow structures identified by the constant Q-criterion (Hunt et al., 1988), as shown in figure 10. Before the start of the pitch-perturbation, the wing has rotated with about the flapping axis with a constant angular velocity and angle $\alpha_0 = 15°$. Hence, a conical leading-edge vortex (LEV) has been formed, which stays close to the wing surface. High magnitudes of suction pressure (i.e. negative p^*) can be observed to be beneath the LEV. Since the pitching axis in this case is closer to the leading edge, as the wing starts pitching up, a major part of the wing, which is below the pitching axis, starts moving downward. As a result of the net downward resultant velocity, the magnitudes of suction on the wing surface increase significantly, for example, at t/T = 0.47. This rise in the suction magnitude is responsible for the higher C_L observed during the pitch-up motion. As the pitch motion decelerates and the wing starts pitching down, the net relative velocity of the lower region of the wing is upwards, which results in the positive p^* in this region. Hence, the net normal force on the wing is also downwards, due to which a negative C_L is observed. As the perturbation ends, the suction pressure on the wing surface is recovered.

The flow structures on the wing undergo significant changes due to pitch perturbation. For better clarity, the normalised spanwise vorticity $[\omega_z^* = \omega_z(0.75R)/U_{ref}]$ contours are plotted on a cross-section plane passing through the wing's midspan, as shown in the bottom row of figure 10. During the pitch-up acceleration, a strong trailing-edge vortex starts to develop, which is separated from the wing at the end of the pitch-up motion at $t/T = 0.52$. During

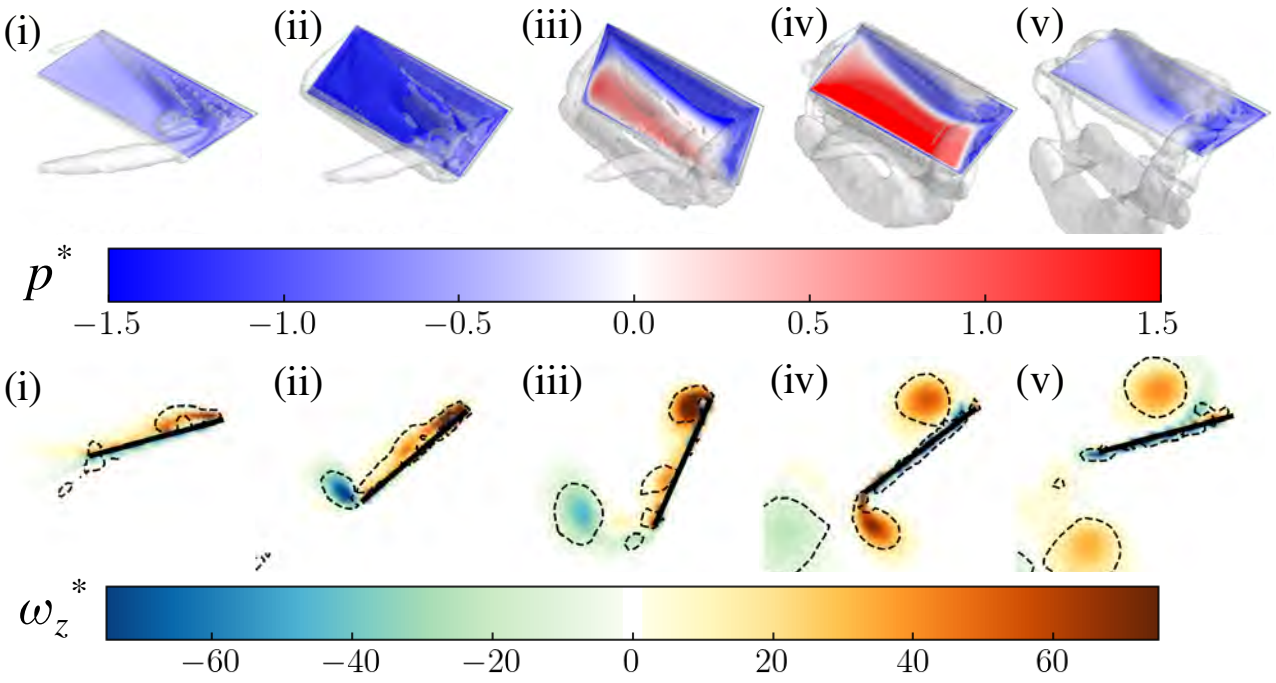

Figure 10: For the wing during its pitch perturbation with $\alpha_0 = 15°$, $\Delta\alpha = 52°$, $\tau = 0.2$, and $\hat{x}_{pa} = 0.2$, the top row shows the normalised pressure (p^*) contours on the wing's suction surface at (i) $t/T = 0.4$, (ii) $t/T = 0.47$, (iii) $t/T = 0.52$, (iv) $t/T = 0.58$, and (v) $t/T = 0.65$. The vortical structures are shown by the semi-transparent isosurfaces of the constant Q criterion. The bottom row shows the normalised spanwise vorticity (ω_z^*) contours over a cross-sectional plane passing through the centre of the wingspan at the same time steps as in the top row. Here, the dashed lines represent the constant Q criterion.

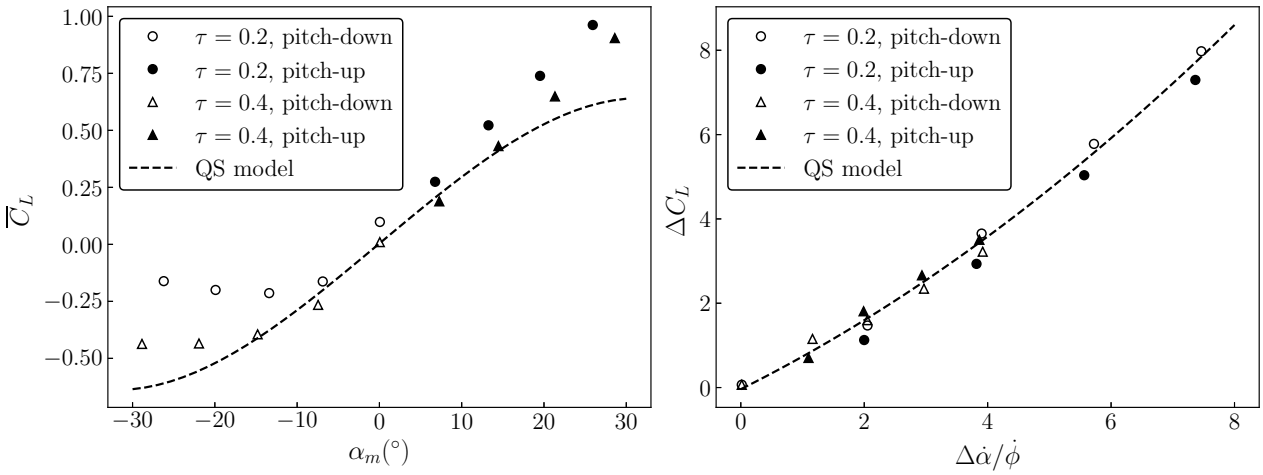

Figure 11: The mean lift coefficient ($\overline{C}_L$) values during the pitch perturbation for various $\Delta\alpha$ and τ cases are plotted as a function of the mean angle of attack α_m in (a). The peak-to-peak variation (ΔC_L) during the perturbation is plotted as a function of the normalised peak-to-peak perturbation angular velocity $\dot{\alpha}/\dot{\phi}$ in (b). The dashed lines represent the predictions of the QS model.

the same time, the LEV is disturbed and is spread over most of the wing suction surface, remaining close to the surface. At $t/T = 0.52$, the pitch-down acceleration is at its peak. Hence, the shear layer on the leading edge forms a stronger LEV than that before the pitch perturbation. Due to the wing's pitch-down motion and increased feeding of vorticity in the LEV, the LEV grows in size and is also lifted away from the wing surface at $t/T = 0.58$ and later. Moreover, an upward motion of the trailing edge also creates a shear, thereby forming a co-rotating trailing-edge vortex as LEV, but on the pressure side of the wing. At the end of pitch perturbation, both corotating vortices move away from the wing surfaces. At this time step, the flow structures around the wing are very different from those before the start of the perturbation. However, the values of C_L and C_D are observed to be similar before and immediately after the perturbation. Hence, the observed changes in the flow structures only minimally affect the forces on the wing. The wing-surface pressures are more related to the wing motion, which can be explained by the rotational effects in the quasi-steady model.

As per the quasi-steady model, the translational effects are proportional to the instantaneous angle α and the rotational effects are proportional to the instantaneous pitch-angular velocity $\dot{\alpha}$. Since the pitch perturbation follows a symmetric profile in α, the mean value of $\dot{\alpha}$ is expected to be 0. Hence, the mean value of C_L (i.e. $\overline{C}_L$) will be independent of $\dot{\alpha}$ and will depend only on the mean α (i.e. α_m). The peak-to-peak variations in C_L (i.e. ΔC_L) will depend on the peak-to-peak variations in $\dot{\alpha}$ (i.e. $\Delta\dot{\alpha}$). This is verified by plotting $\overline{C}_L$ against α_m and ΔC_L against $\dot{\alpha}/\dot{\phi}$ for the data obtained from various pitching amplitudes, durations, and both pitch-up and pitch-down motions, as shown in figure 11.

The values of $\overline{C}_L$ in all cases are close to the trend predicted by the quasi-steady model in figure 11(a). The experimental uncertainty in measuring small forces might account for the difference observed between the values and the trend line. Similarly, the values of $\Delta\dot{\alpha}$ show a close fit to the trend line obtained from the quasi-steady model in figure 11(b). Note that the pitch-angular velocity in all perturbed cases is greater than the flapping velocity $\dot{\phi}$.

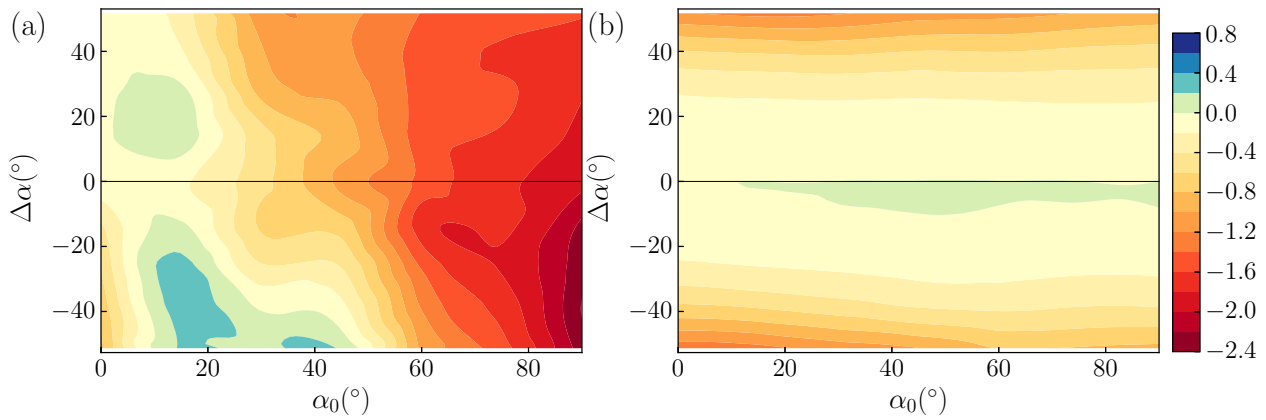

Figure 12: The contours of the time-averaged coefficients of (a) flapping power ($\overline{C}_{P,flap}$) and (b) pitching power ($\overline{C}_{P,pitch}$) are shown on the maps of α_0 and $\Delta\alpha$ for the cases with $\tau = 0.2$ and $\hat{x}_{pa} = 0.2$.

Hence, the effects of pitch rotation on C_L are significantly higher than the translational effects. The overlap of data from various cases, for example, at $\dot{\alpha}/\dot{\phi} = 4$ demonstrates that, despite undergoing pitch perturbations with different amplitudes and duration, the same $\dot{\alpha}$ should result in the same variations in C_L. In conclusion, the instantaneous forces on the wing are highly sensitive to the pitch-rotation velocity, whereas the average performance is dependent on the translational effects only.

Finally, the coefficient of power transferred from the fluid to the wing was calculated as

$$C_P = \frac{\tau_y \dot{\phi} + \tau_z \dot{\alpha}}{0.5\rho U_{ref}^3 A}, \tag{13}$$

where τ_y and τ_z are the torques around the flapping and pitching axes, respectively. Accordingly, the flapping and pitching powers can be separated as $C_P = C_{P,flap} + C_{P,pitch}$. For various values of α_0 and $\Delta\alpha$ explored in this work, the mean power transfer coefficients $\overline{C}_{P,flap}$ and $\overline{C}_{P,pitch}$ during the perturbation were computed for all the cases with $\tau = 0.2$ and $\hat{x}_{pa} = 0.2$. The values of those power coefficients were plotted as contours on the maps of α_0 and $\Delta\alpha$, as shown in figure 12. The flapping power is observed to be dependent on both α_0 and $\Delta\alpha$, whereas the pitching power is only the function of $\Delta\alpha$, irrespective of α_0. This is because the flapping torque τ_y depends on the drag acting on the wing that changes with both α_0 and $\Delta\alpha$. On the other hand, the pitching torque τ_z depends largely on the force normal to the wing surface, which depends on $\dot{\alpha}$ as described by the rotational components of the quasi-steady model. In all these cases, τ is maintained constant. Hence, $\dot{\alpha}$ is varied with $\Delta\alpha$, which changes the normal force and hence, the mean flapping power.

The region bounded by $10° \leq \alpha_0 \leq 30°$ and $-20° \leq \Delta\alpha \leq -50°$ in figure 12(a) might be of interest since it shows positive power transfer from the fluid to the wing. This indicates the possibility of the wing being self-propelled about the flapping axis. It should be noted that these values are within the uncertainty of the experiments. Nevertheless, the possibility of reduced drag or improved flapping efficiency around this region may be explored in future.

1.5 Conclusions

The effects of pitch perturbations on a rotating wing were studied, both experimentally and numerically, by providing a single pitch perturbation during its rotation with a constant angular velocity. The initial angle, amplitude and duration of perturbation were systematically varied. Without a perturbation, wings rotating at a constant Reynolds number and set at a constant angle were known to experience constant lift and drag due to the stable attachment of the leading-edge vortex. However, the stability was observed to be severely affected during the pitch perturbation. The magnitudes of changes in the lift and drag coefficients were found to be sensitive to the initial angle. The variations in the aerodynamic forces were found to be due to the rotational effects explained by the quasi-steady model of Lee et al. (2016). The rotational effects were dependent on the pitch rotational velocity, which was modified by changing the amplitude and duration of perturbations in different sets of experiments. An increase in the pitch-rotational velocity was found to result in an increase in the hysteresis in the variation in the lift as a function of the wing angle. The rotational effects were dependent on the pitch-axis location, which could be increased by moving the pitch axis closer to the leading edge. However, the mean lift and drag remained unaffected, being dependent only on the translational effects. The lift and drag returned to their stable values immediately after the perturbation, irrespective of the significant changes in the flow structure around the wing. Thus, the quasi steady effects due to pitch rotation dominated the instantaneous forces. Finally, the analysis of the power transfer between the fluid and the wing showed that the pitching power relied only on the perturbation velocity, whereas the flapping power relied on both the initial angle and the perturbation velocity. Moreover, some pitch-down perturbations showed a possibility of improved power economy, which may be explored in detail in future.

2 Streamline penetration, velocity error and consequences of the feedback immersed boundary method

2.1 Introductions

The immersed boundary method (IBM) has attracted growing interest in the computational fluid dynamics (CFD) research community due to its simplicity in dealing with fluid-structure interaction (FSI) systems involving complex geometries and large deformations (Mittal and Iaccarino, 2005; Sotiropoulos and Yang, 2014; Huang and Tian, 2019). The IBM was first developed by Peskin (1972) for modelling FSI of heart flows. In this method, the fluid dynamics is solved on a fixed Cartesian grid that does not conform to the fluid-structure boundaries, significantly reducing the effort in mesh generation and avoiding the mesh movement for moving boundaries. A boundary force density (also known as Lagrangian force) is distributed to the fluid (also known as Eulerian body force density) in the vicinity of the moving boundaries to account for their interactions (Peskin, 1972; Mittal and Iaccarino, 2005; Sotiropoulos and Yang, 2014). The Lagrangian force is calculated by considering the principle of virtual work of the elastic body, i.e., $\boldsymbol{F}_{ib} = -\delta E/\delta \boldsymbol{X}$, where E is the elastic energy function at the boundary configuration $\boldsymbol{X}$ (Peskin, 2002; Huang and Tian, 2019). The fluid dynamics is described in the Eulerian form while the boundary is tracked in the Lagrangian form for the convenience of treating moving boundary cases (Peskin, 1972; Mittal and Iaccarino, 2005).

Since Peskin's pioneer work, great effort has been made in improving the capability of the IBM. For example, Goldstein et al. (1993) extended the IBM by introducing a feedback forcing scheme with two feedback coefficients α and β, so that the Eulerian body force density $\boldsymbol{f} = \alpha \int_0^t \mathbf{u}(\tau)d\tau + \beta \mathbf{u}(t)$, where $\mathbf{u}$ is the fluid velocity around the boundary. This scheme is efficient and can be used to simulate complex-geometry and turbulent flows (Goldstein et al., 1993; Huang and Tian, 2019). From the physical point of view, the α term acts like a spring force on a small volume of fluid around the boundary; and the β term provides a damping effect (Goldstein et al., 1993; Mittal and Iaccarino, 2005). The two feedback coefficients should be large enough to maintain the accuracy and small enough to avoid a system with a very large stiffness to ensure the numerical stability (Goldstein et al., 1993; Sui et al., 2007; Huang and Sung, 2009; Ji et al., 2012; Sotiropoulos and Yang, 2014; Huang and Tian, 2019). A direct-forcing IBM was proposed by Mohd-Yusof (1997) and Fadlun et al. (2000). In this method, the body force density is directly deduced from the momentum equation, which can be taken as a special version of the feedback IBM. As a result, the feedback coefficients are fixed. On the other hand, several sharp-interface IBMs have been developed and applied to many topics such as fish swimming, insect/bird flight and cardiovascular flows (Borazjani and Sotiropoulos, 2008; Mittal et al., 2008; Song et al., 2014; Tian et al., 2014a; Zhu et al., 2014; Mittal et al., 2016). While sharp-interface IBMs have higher-order accuracy, special techniques are required to reduce the numerical oscillations due to the violation of the geometric conservation law near the immersed boundary (Seo and Mittal, 2011; Luo et al., 2012). Mittal and Bhardwaj (2022) recently reviewed the progress in the development and application of diffused-interface and sharp-interface IBMs to thermofluids problems and discussed their computational challenges.

To improve the computational efficiency, the IBM was combined with the lattice Boltzmann method (LBM) by Feng and Michaelides (2004) to simulate fluid–particles interactions. The immersed boundary-lattice Boltzmann method (IB-LBM) has since been implemented in many applications, including blood flow (Krüger et al., 2011; Huang et al., 2021b), viscoelastic fluids

with complex geometries (Zhu, 2018; Ma et al., 2020), fish swimming (Sui et al., 2007; Tian et al., 2011; Zhu et al., 2021), flapping wings (Liu et al., 2017; Huang et al., 2021a), and flows at moderate and high Reynolds numbers (Xu et al., 2018; Cheylan et al., 2021). In addition, a direct-forcing IB-LBM was also developed (Feng and Michaelides, 2005; Sui et al., 2007; Dupuis et al., 2008).

Although the feedback IBM (including the direct-forcing version) has the advantage of simplicity, its accuracy and streamline penetration have been widely discussed (Luo et al., 2007; Kang and Hassan, 2011; Zhang et al., 2016; Cai et al., 2018; Tao et al., 2019a; Jiang and Liu, 2019; Peng and Wang, 2020; Gsell and Favier, 2021; Zhao et al., 2021). Several strategies have been proposed to enhance velocity accuracy near the immersed boundary, such as introducing an iterative IBM (also known as multi-direct forcing IBM) into LBM (Suzuki and Inamuro, 2011) and implicit IB-LBM (Wu and Shu, 2009). The iterative IB-LBM iterates the IBM calculation until the velocity error less than a prescribed threshold. Zhang et al. (2020) showed that usually, five iterations are required to accurately enforce the no-slip boundary condition for flow over a stationary cylinder. In many of the above works, obvious penetration of streamlines through the fluid-solid interface that was generated by their original feedback IBM implementation has been reported. However, our simulations have not observed such severe violations of the no-slip and no-penetration velocity boundary conditions. Therefore, we aim to provide an important guideline for the correct use of the feedback IBMs by comparing the performance of three implementations in modelling a few benchmark cases. In addition, the consequences of the boundary velocity error and the spurious flow penetration have not been discussed, especially for internal flows. These are the motivations for this study.

In this study, we compare the non-iterative IBMs with and without the prediction step and the iterative IB-LBM to clarify the source of streamline penetration and correct the implementation of the IBM. In addition, we discuss the velocity error and the spurious flow penetration and their consequences in external and internal flows. This study will provide an important guideline for the correct use of the feedback IBM.

The remaining parts of this paper are organized as follows: Sec. 2.2 introduces three implementations of the feedback IB-LBM. Then, detailed case testings of the numerical method and discussions are provided in Sec. 2.6. Finally, conclusions are given in Sec. 2.7.

2.2 Numerical methods

In this study, the lattice Boltzmann method (LBM) with the multi-relaxation-time (MRT) model is adopted for the fluid dynamics. For two-dimensional (2-D) FSI cases (e.g. flow-induced vibration of a flexible plate attached behind a stationary cylinder in a channel and a one-sided collapsible channel), the nonlinear dynamics of the structure is treated as a Bernoulli-Euler beam and solved by the finite difference method (FDM). In the three-dimensional (3-D) FSI case, the nonlinear dynamics of the structure is solved by the finite element method (FEM). The two-way fluid-structure interaction is implemented by the feedback IBM. The details of these methods are given in the following subsections. For simplicity, only the 2-D numerical method is presented; the extension to 3-D is straightforward, which can be also found in our previous publications (Huang et al., 2021a,b,c; Huang, 2021).

2.3 Fluid solver

The governing equations for the incompressible fluid flow are,

$$\nabla \cdot \boldsymbol{u} = 0, \tag{14}$$

$$\rho \frac{\partial \boldsymbol{u}}{\partial t} + \rho \boldsymbol{u} \cdot \nabla \boldsymbol{u} = -\nabla p + \mu \nabla^2 \boldsymbol{u} + \boldsymbol{f}, \tag{15}$$

where $\boldsymbol{u}$ is the fluid velocity, ρ is the fluid density, p is the pressure, μ is the dynamic viscosity, and $\boldsymbol{f}$ is the body force density. In the LBM, the computational domain is discretised with a fixed Eulerian grid (lattice grid). The fluid is modelled as a set of fictive particles undergoing streaming and collision over a lattice grid. The macroscopic dynamics of the fluid is the result of the statistical behaviour of the particles, which is described by the distribution function $g_i(\boldsymbol{x}, t)$ according to (Lallemand and Luo, 2000; Luo et al., 2011)

$$g_i(\boldsymbol{x} + \boldsymbol{e}_i \Delta t, t + \Delta t) - g_i(\boldsymbol{x}, t) = \Omega_i(\boldsymbol{x}, t) + \Delta t G_i, \tag{16}$$

where $g_i(\boldsymbol{x}, t)$ is the distribution function for particles with velocity $\boldsymbol{e}_i$ at position $\boldsymbol{x}$ and time t, Δt is the time increment, $\Omega_i(\boldsymbol{x}, t)$ is the collision operator, and G_i is the forcing term accounting for the body force $\boldsymbol{f}$. The D2Q9 model is used on a square lattice. "D2" stands for "2 dimensions", while "Q9" stands for "9 particle speeds". The discrete velocity components of D2Q9 model can be represented as

$$\begin{aligned}
&\boldsymbol{e_0} = (0, 0), \\
&\boldsymbol{e_i} = (\cos[\pi(i-1)/2], \sin[\pi(i-1)/2]) c_\Delta, i = 1-4, \\
&\boldsymbol{e_i} = \sqrt{2}(\cos[\pi(i-9/2)/2], \sin[\pi(i-9/2)/2]) c_\Delta, i = 5-8,
\end{aligned} \tag{17}$$

where $c_\Delta = \Delta x / \Delta t$ with Δx the lattice spacing. Compared to the single relaxation time (SRT) collision model, the multiple relaxation time (MRT) model has been proven to be more numerically stable owing to shear and bulk viscosities are allowed to tune independently (Lallemand and Luo, 2000). Increasing the bulk viscosity can often improve the numerical stability by attenuating any spurious pressure waves more quickly(Krüger et al., 2017). Therefore, the MRT collision model is adopted here and is given by Lallemand and Luo (2000),

$$\Omega_i = -(\boldsymbol{M}^{-1} \boldsymbol{S} \boldsymbol{M})_{ij} [g_i(\boldsymbol{x}, t) - g_i^{eq}(\boldsymbol{x}, t)], \tag{18}$$

where $\boldsymbol{M}$ is a 9×9 transform matrix, and $\boldsymbol{S} = \mathrm{diag}(s_0, s_1, \ldots, s_8)$ is a non-negative diagonal 9×9 relaxation matrix for D2Q9 model. In matrix $\boldsymbol{S}$, s_1 is related to the bulk viscosity of the fluid, s_7 and s_8 are related to the shear viscosity of the fluid, and other parameters are free parameters. The physical meaning and valuesof these parameters be found in Lallemand and Luo (2000) and Luo et al. (2011). The equilibrium distribution function g_i^{eq} is defined as

$$g_i^{eq} = \rho \omega_i \Big[1 + \frac{\boldsymbol{e_i} \cdot \boldsymbol{u}}{c_s^2} + \frac{\boldsymbol{u}\boldsymbol{u} : (\boldsymbol{e}_i \boldsymbol{e}_i - c_s^2 \boldsymbol{I})}{2 c_s^4} \Big], \tag{19}$$

where $c_s = \Delta x / (\sqrt{3} \Delta t)$ is the speed of sound, $\boldsymbol{I}$ is the unit tensor, and the weighting factors ω_i are given by $\omega_0 = 4/9$, $\omega_{1-4} = 1/9$ and $\omega_{5-8} = 1/36$. The mass density ρ, pressure p, and velocity $\boldsymbol{u}$ are respectively calculated by

$$\rho = \sum_i g_i, \quad p = \rho c_s^2, \quad \boldsymbol{u} = \left(\sum_i \mathbf{e}_i g_i + \frac{1}{2} \boldsymbol{f} \Delta t \right) \Big/ \rho. \tag{20}$$

The force scheme proposed by Guo et al. Guo et al. (2002) is adopted to determine G_i,

$$G_i = [\boldsymbol{M}^{-1}(\boldsymbol{I} - \boldsymbol{S}/2)\boldsymbol{M}]_{ij}F_i, \tag{21}$$

$$F_i = \left(1 - \frac{1}{2\tau}\right)\omega_i\left[\frac{\boldsymbol{e}_i - \boldsymbol{u}}{c_s^2} + \frac{\boldsymbol{e}\cdot\boldsymbol{u}}{c_s^4}\boldsymbol{e}_i\right]\cdot\boldsymbol{f}, \tag{22}$$

where $\tau = 1/s_8$ is the non-dimensional relaxation time.

2.4 Structure solver

The geometrically nonlinear dynamics of a 2-D elastic wall is described by the Bernoulli-Euler beam (Connell and Yue, 2007; Huang, 2021),

$$\rho_s\frac{\partial^2\boldsymbol{X}}{\partial t^2} = \frac{\partial}{\partial s}\left[T(s)\frac{\partial\boldsymbol{X}}{\partial s}\right] - EI\frac{\partial^4\boldsymbol{X}}{\partial s^4} + \boldsymbol{F}, \tag{23}$$

where ρ_s is the linear density of the elastic wall, s is the arc length along the elastic wall, $\boldsymbol{X}$ is the position vector of the Lagrangian point on the elastic wall, $T(s)$ is the longitudinal tension, EI is the bending stiffness (where E is the Young's modulus, $I = h^3/12$ is the moment of inertia of the wall cross-section and h is the wall thickness), and $\boldsymbol{F}$ is the hydrodynamic stress exerted by the fluid. The longitudinal tension $T(s)$ is evaluated by the Hooke's law

$$T(s) = Eh\left(\left|\frac{\partial\boldsymbol{X}}{\partial s}\right| - 1\right), \tag{24}$$

where Eh is the stretching stiffness. In this study, the FDM is used to discretize the governing equation (i.e. Eq. 23) of the elastic wall. The mesh size of the solid wall is half of the lattice spacing to avoid "fluid volume leakage"(Peskin, 2002; Krüger et al., 2017; Huang and Tian, 2019). The details of the numerical method can be found in Huang (2021) and Ma et al. (2020).

2.5 Feedback immersed boundary method

The two-way interactions between the fluid and the structure are coupled by the feedback law (Kim and Peskin, 2007),

$$\boldsymbol{F}_{ib}(s,t) = \beta\rho(\boldsymbol{x},t)(\boldsymbol{U}(s,t) - \boldsymbol{U}_{ib}(s,t)), \tag{25}$$

where $\boldsymbol{F}_{ib}(s,t)$ is the Lagrangian force density, β is the feedback coefficient and $\beta = 2m/s$ in LBM simulations, $\boldsymbol{U}_{ib}(s,t)$ is the immersed boundary velocity interpolated from the ambient flow, and $\boldsymbol{U}(s,t)$ represents the velocity of the solid wall, $\boldsymbol{U}(s,t) = 0$ for a rigid solid wall. In dimensionless form $\beta^* = \beta/U_0 = 40$, and β^* ranges from 20 to 104 (Huang et al., 2021b). It is noted that this method is simple, and has been extensively used in both laminar and turbulent flows (see e.g. Refs. [Xu et al. (2018); Huang and Tian (2019); Huang et al. (2021b)]).

A Dirac delta function is used to transfer the interactions between the Lagrangian and Eulerian variables. The velocity interpolation and Lagrangian force distribution to the adjacent Eulerian grid points are calculated according to

$$\boldsymbol{U}_{ib}(s,t) = \int \boldsymbol{u}(x,t)\delta(\boldsymbol{x} - \boldsymbol{X}(s,t))d\boldsymbol{x}, \tag{26}$$

Algorithm 1: conventional feedback IB-LBM

1. Initialize the computation parameters.
2. Interpolate the immersed boundary velocity $\boldsymbol{U}_{ib}$ using Eq. (26).
3. Compute the Lagrangian force density $\boldsymbol{F}_{ib}(s,t)$ using Eq. (25).
4. Spread $\boldsymbol{F}_{ib}(s,t)$ to the Eulerian lattice to obtain $\boldsymbol{f}(\boldsymbol{x})$ using Eq. (27).
5. Perform the collision step with the Eulerian body force $\boldsymbol{f}(x)$.
6. Stream the distribution function to neighbouring nodes to obtain g_i: $g_i\left(\boldsymbol{x}+\boldsymbol{e}_i\Delta t, t+\Delta t\right) = g_i\left(\boldsymbol{x}, t\right)$.
7. Compute the macroscopic variables: density ρ, pressure p, and the velocity $\boldsymbol{u}$ using Eq. (20).
8. Calculate g_i^{eq} using Eq. (19).
9. Go to step 2 for next time-step.

$$\boldsymbol{f}(\boldsymbol{x},t) = \int \boldsymbol{F}_{ib}(s,t)\delta(\boldsymbol{x}-\boldsymbol{X}(s,t))ds, \tag{27}$$

where $\boldsymbol{u}(x,t)$ is the fluid velocity, $\boldsymbol{x}$ is the coordinate of the fluid lattice nodes, $\delta(\boldsymbol{x}-\boldsymbol{X}(s,t))$ is Dirac delta function, $\boldsymbol{X}$ is the coordinate of the solid wall, $\boldsymbol{f}$ is the body force added in the Navier-Stokes equation to mimic a boundary condition, and ds is the arc length of the immersed boundary.

Because the location of the immersed boundary does not generally coincide with the nodal points of the Cartesian grid, the boundary force need to be distributed over a band of lattices around each Lagrangian point, resulting in a diffusive boundary (Mittal and Iaccarino, 2005). The Dirac delta function is a smooth distribution function, serving as a Gaussian like function in transferring boundary information between Lagrangian and Eulerian points. The 4-point discrete delta function $\delta_h(\boldsymbol{x}-\boldsymbol{X}(s,t))$ developed by Peskin (2002) is used to approximate the Dirac delta function,

$$\delta_h(\boldsymbol{x}-\boldsymbol{X}(s,t)) = \frac{1}{\Delta x\Delta y}\phi\left(\frac{x-X(s,t)}{\Delta x}\right)\phi\left(\frac{y-Y(s,t)}{\Delta y}\right), \tag{28}$$

$$\phi(r) = \begin{cases} \frac{1}{8}\left(3-2|r|+\sqrt{1+4|r|-4r^2}\right), & 0\le|r|\le 1, \\ \frac{1}{8}\left(5-2|r|-\sqrt{-7+12|r|-4r^2}\right), & 1\le|r|\le 2, \\ 0, & |r|>2, \end{cases} \tag{29}$$

where $r = (x-X(s,t))/\Delta x$ for x-component, and $(y-Y(s,t))/\Delta y$ for y-component.

Here we consider three implementations of the feedback IB-LBM, summarized in Algorithms 1, 2 and 3. Algorithm 1 is the conventional feedback IB-LBM without a prediction step. Algorithm 2 is an improved IB-LBM with a prediction step. Algorithm 3 is an iterative feedback IB-LBM. Algorithm 1 could be taken as a special case of Algorithm 3 with 1 iteration. Algorithm 2 can be taken as a variation of Algorithm 1 by slightly modifying the integration scheme. The computational complexities of Algorithms 1, 2 and 3 are, respectively, $O(N)$, $O(N)$ and $O(mN)$, where N is the number of the Lagrangian points and m is the total iteration number, see also Zhao et al. (2021). For each algorithm, a partitioned and weakly coupled approach of the fluid and structure solvers is adopted, where each solver is solved sequentially only once at each time step. Consequently, the fluid-solid interface boundary conditions are mismatched by one-half step at the end of each time step. This approach is computationally

Algorithm 2: improved feedback IB-LBM

1. Initialize the computation parameters.
2. Stream the distribution function to neighbouring nodes to obtain g_i: $g_i\left(\boldsymbol{x}+\boldsymbol{e}_i\Delta t, t+\Delta t\right)=g_i\left(\boldsymbol{x}, t\right)$.
3. **Prediction step:** compute the macroscopic variables density ρ and the uncorrected velocity $\boldsymbol{u}$ using $\rho=\sum_i g_i, \quad \boldsymbol{u}=1/\rho\sum_i \boldsymbol{e}_i g_i$.
4. Interpolate the immersed boundary velocity $\boldsymbol{U}_{ib}$ using Eq. (26).
5. Compute the Lagrangian force density $\boldsymbol{F}_{ib}(s,t)$ using Eq. (25).
6. Spread $\boldsymbol{F}_{ib}(s,t)$ to the Eulerian lattice to obtain $\boldsymbol{f}(\boldsymbol{x})$ using Eq. (27).
7. Calculate g_i^{eq} using Eq. (19).
8. Perform the collision step with the Eulerian body force $\boldsymbol{f}(x)$.
9. Correct the Eulerian velocity near to the immersed boundary according to $\boldsymbol{u}(\boldsymbol{x})=\boldsymbol{u}(\boldsymbol{x})+\boldsymbol{f}(\boldsymbol{x})\Delta t/2\rho(\boldsymbol{x})$.
9. Go to step 2 for next time-step.

efficient, while it may cause numerical instability at low structure-to-fluid mass ratios (Tian et al., 2014a; Huang et al., 2021b). To improve the numerical stability, an iterative feedback IBM, as shown in Algorithm 3, is used at the fluid-solid interface, which allows for local flow reconstruction near the solid boundary. The iteration ensures that the displacement, velocity and traction boundary conditions at the fluid-solid interface are matched between the fluid and the solid boundary at each time step (Huang et al., 2021b). Note that in Algorithm 3, the pre-ste criterion is an empirical parameter. At low structure-to-fluid mass ratios, the numerical stability can also be improved by implicit/strong coupling (Mittal and Bhardwaj, 2022).

Algorithm 3: iterative feedback IB-LBM

1. Initialize the computation parameters.
2. Stream the distribution function to neighbouring nodes to obtain g_i: $g_i\left(\boldsymbol{x}+\boldsymbol{e}_i\Delta t, t+\Delta t\right)=g_i\left(\boldsymbol{x}, t\right)$.
3. **Prediction step:** compute the macroscopic variables density ρ and the uncorrected velocity $\boldsymbol{u}$ using $\rho=\sum_i g_i, \quad \boldsymbol{u}=1/\rho\sum_i \boldsymbol{e}_i g_i$.
4. Set iteration number (m) of IBM to 0 and repeat for each time step.
5. Iteration loop:
   (1) Interpolate the immersed boundary velocity $\boldsymbol{U}_{ib}^m$ using Eq. (26).
   (2) Compute the Lagrangian force density $\boldsymbol{F}_{ib}^m(s,t)$ using Eq. (25).
   (3) Spread $\boldsymbol{F}_{ib}^m(s,t)$ to the Eulerian lattice to obtain $\boldsymbol{f}^m(\boldsymbol{x})$ using Eq. (27).
   (4) Correct the Eulerian velocity near to the immersed boundary according to $\boldsymbol{u}^{m+1}(\boldsymbol{x})=\boldsymbol{u}^m(\boldsymbol{x})+\boldsymbol{f}^m(\boldsymbol{x})\Delta t/2\rho(\boldsymbol{x})$.
   (5) Update iteration number $m=m+1$.
6. Repeat step 5 until m reaches the given maximum iterations or the velocity error at the immersed boundary is less than a pre-set criterion.
7. Calculate g_i^{eq} using Eq. (19).
8. Perform the collision step with the total Eulerian body force: $\boldsymbol{f}(x)=\sum_{m=1}^{m_{max}}\boldsymbol{f}^m(\boldsymbol{x})$.
9. Go to step 2 for next time-step.

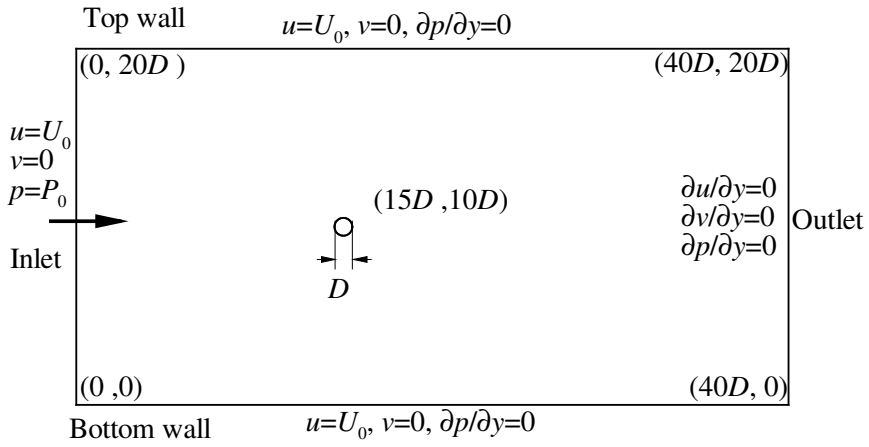

Figure 13: Schematic diagram of a uniform flow over a stationary cylinder.

2.6 Results and Discussion

The flow over a cylinder, flow-induced vibration of a flexible plate attached behind a stationary cylinder in a channel, the flow through a 2-D asymmetric stenosis, a one-sided collapsible channel and a 3-D collapsible tube are conducted here to test the proposed methods. Note that two typical groups of cases are particularly covered: internal/confined and external flows including both steady and unsteady flows. As detailed below, the Reynolds numbers considered are not arranged to be uniform across the cases presented, as the focus here is on the streamline penetration, velocity error and consequences of three implementations of IBM in different types of flows.

2.6.1 Flow over a cylinder

A uniform flow past a 2-D cylinder is one of the most robust methods used for validating the fluid solvers (Canuto and Taira, 2015). Therefore, this problem is used as a benchmark test for the three algorithms. Fig. 13 shows a schematic depiction for the simulation of the flow over the cylinder with boundary conditions and dimensions used. Note that in this work, we only consider flows at low Reynolds numbers, and thus do not implement the non-reflecting boundary condition at the outlet.

The Reynolds number Re, based on the cylinder diameter D, undisturbed free-stream velocity U_0, fluid density ρ and dynamic viscosity μ, determines the flow pattern and drag on a cylinder,

$$Re = \frac{\rho U_0 D}{\mu}. \tag{30}$$

The non-dimensional drag C_D and lift C_L coefficients are defined to describe the hydrodynamic forces on the cylinder,

$$C_D = \frac{F_D}{0.5\rho U_0^2 D}, \quad C_L = \frac{F_L}{0.5\rho U_0^2 D}, \tag{31}$$

where F_D and F_L are the drag and lift forces, respectively. The F_D and F_L are integrated

from the forces exerted on the immersed boundary by the ambient fluid,

$$F_D = \int F_x ds = \sum_{i=1}^{n} F_x^i \Delta s, \quad F_L = \int F_y ds = \sum_{i=1}^{n} F_y^i \Delta s, \tag{32}$$

where F_x^i and F_y^i are the forces acting on the i-th IB point in $x-$ and $y-$directions, and Δs is the cylinder mesh size.

A multi-block LBM (Yu et al., 2002) is adopted to provide high resolution near the cylinder while remaining low resolution in the far-field to reduce the computational effort. Here two blocks of the fluid mesh are used. The finest mesh size around the cylinder is $D/100$. The cylinder mesh size is maintained at half of the fluid mesh. The flow over the cylinder has been simulated at Re = 40, corresponding to a steady flow regime. It respectively requires 5.083, 4.633, and 4.25 CPU min for Algorithm 1, 2 and 3 for calculating 1000 time steps.

We first compare the streamlines of the three implementations of the feedback IB-LBM with the conventional feedback coefficient $\beta = 2m/s$ and the optimal (in practical meaning) feedback coefficient $\beta = 5.2m/s$ where the conventional feedback coefficient is amplified 2.6 times. Here $U_0 = 0.05m/s$ is used for all tested cases. Therefore, the non-dimensional feedback coefficient $\beta^* = \beta/U_0 = 40$ for $\beta = 2m/s$, and $\beta^* = 104$ for $\beta = 5.2m/s$. Fig. 14(a) shows that the streamlines exhibit symmetrical vortices behind the cylinder. The vortex centre location (a, b) is defined as an indication of the consequences of the streamline penetration which will be discussed in Table 1. Figs. 14(b)- 14(h) show the streamlines for the Algorithm 1, Algorithm 2 and Algorithm 3, respectively. As is shown in Fig. 14(b), many streamlines penetrate through the cylinder (i.e. spurious flow penetration as described by He et al. He et al. (2021)) for the conventional feedback IB-LBM (Algorithm 1, $\beta = 2m/s$), which means the no-penetration boundary condition is not precisely satisfied at the fluid-solid interface. Fig. 14(c) shows that the apparent streamline penetration still exists for Algorithm 1 with $\beta = 5.2m/s$. Similar spurious flow penetration can be also found in the improved (Algorithm 2, $\beta = 2m/s$) and the 1 iteration (Algorithm 3, $\beta = 2m/s$) feedback IB-LBM (i.e. Figs. 14(d) and 14(f)). In contrast, there is no streamline penetration through the cylinder for the improved (Algorithm 2, $\beta = 5.2m/s$) and 5 iterations (Algorithm 3, $\beta = 2m/s$) feedback IB-LBM (i.e. Figs. 14(e) and 14(g))). Fig. 14(h) shows that there is also no streamline penetration through the cylinder for the 1 iteration (Algorithm 3) feedback IB-LBM with $\beta = 5.2m/s$.

The observations suggest that either iterations or a larger feedback coefficient can suppress the spurious flow penetration and improve the no-penetration boundary condition at the fluid-solid interface. These observations have also been reported in previous studies (Kang and Hassan, 2011; Cai et al., 2018; Tao et al., 2019a,b). Compared with Algorithm 1, the velocity prediction step in Algorithm 2 and Algorithm 3 can help to suppress the spurious flow penetration and reduce the velocity slip on the immersed boundaries.

Table 1 shows the results from the present simulation and those published in the literature for comparisons. A reasonably good agreement is found between the present results and other numerical simulations and experimental results for all quantities of interest. For the vortex centre location (a, b) and drag coefficient C_D computed by present three algorithms, the difference is negligibly small, indicating that iterations do not significantly improve the prediction of the drag and the vortex centre location. In the rest of this paper, we only compare Algorithm 3 for different iteration strategies and feedback coefficients.

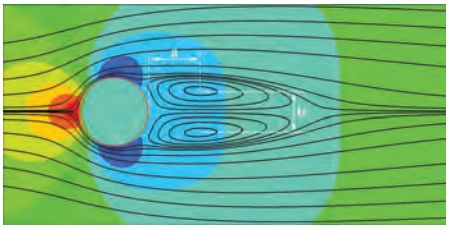

(a) Vortex centre location

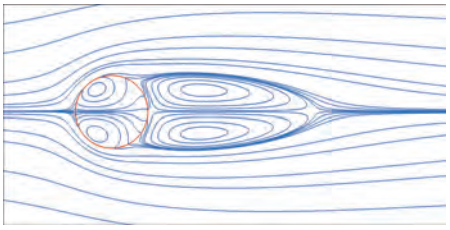

(b) Algorithm 1: $\beta = 2m/s$

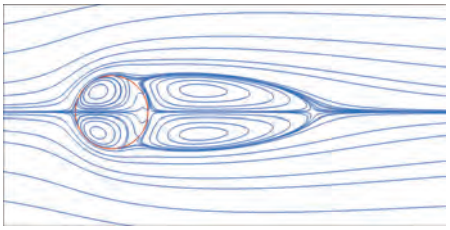

(c) Algorithm 1: $\beta = 5.2m/s$

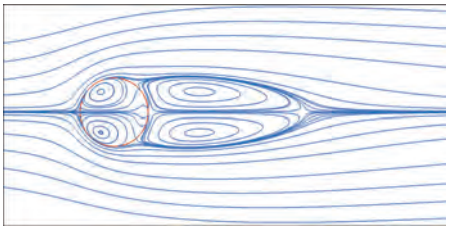

(d) Algorithm 2: $\beta = 2m/s$

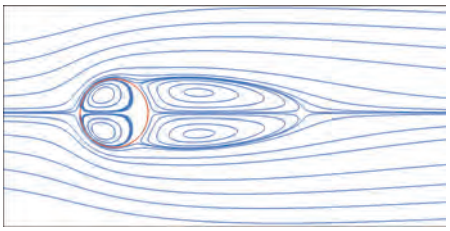

(e) Algorithm 2: $\beta = 5.2m/s$

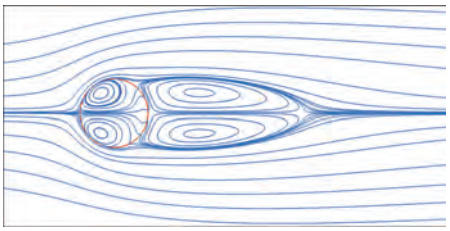

(f) Algorithm 3: 1 iteration, $\beta = 2m/s$

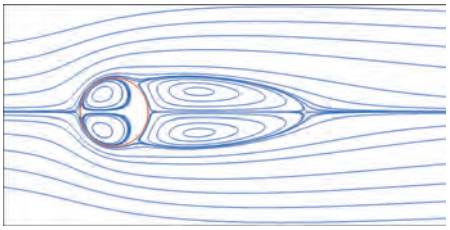

(g) Algorithm 3: 5 iterations, $\beta = 2m/s$

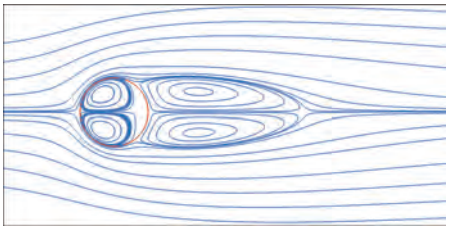

(h) Algorithm 3: 1 iteration, $\beta = 5.2m/s$

Figure 14: Streamlines for flow over a stationary cylinder at $Re = 40$: (a) the definition of the vortex centre location (a, b) as an indication of the consequences of the streamline penetration which will be discussed in Table 1; (b) Algorithm 1, $\beta = 2m/s$; (c) Algorithm 1, $\beta = 5.2m/s$; (d) Algorithm 2, $\beta = 2m/s$; (e) Algorithm 2, $\beta = 5.2m/s$; (f) Algorithm 3: 1 iteration, $\beta = 2m/s$; (g) Algorithm 3: 5 iterations, $\beta = 2m/s$; (h) Algorithm 3: 1 iteration, $\beta = 5.2m/s$. Note: $U_0 = 0.05m/s$ is used for all tested cases. Therefore, the non-dimensional feedback coefficient $\beta^* = \beta/U_0 = 40$ for $\beta = 2m/s$, and $\beta^* = 104$ for $\beta = 5.2m/s$.

Table 1: For $Re = 40$, a uniform flow over a stationary cylinder: vortex centre location (a, b), and drag coefficient C_D. Note: $U_0 = 0.05m/s$ is used for all tested cases. Therefore, the non-dimensional feedback coefficient $\beta^* = \beta/U_0 = 40$ for $\beta = 2m/s$, and $\beta^* = 104$ for $\beta = 5.2m/s$.

Sources	a/D	b/D	C_D
Tritton (1959)	–	–	1.59
Coutanceau and Bouard (1977)	0.76	0.59	–
Linnick and Fasel (2005)	0.72	0.60	1.61
Berthelsen and Faltinsen (2008)	0.72	0.60	1.59
Wang et al. (2017)	0.75	0.60	1.65
Algorithm 1: $\beta = 2m/s$	0.74	0.60	1.62
Algorithm 1: $\beta = 5.2m/s$	0.73	0.60	1.61
Algorithm 2: $\beta = 2m/s$	0.74	0.60	1.61
Algorithm 2: $\beta = 5.2m/s$	0.73	0.60	1.60
Algorithm 3: 1 iteration, $\beta = 2m/s$	0.74	0.60	1.61
Algorithm 3: 5 iterations, $\beta = 2m/s$	0.73	0.60	1.60
Algorithm 3: 1 iteration, $\beta = 5.2m/s$	0.73	0.60	1.60

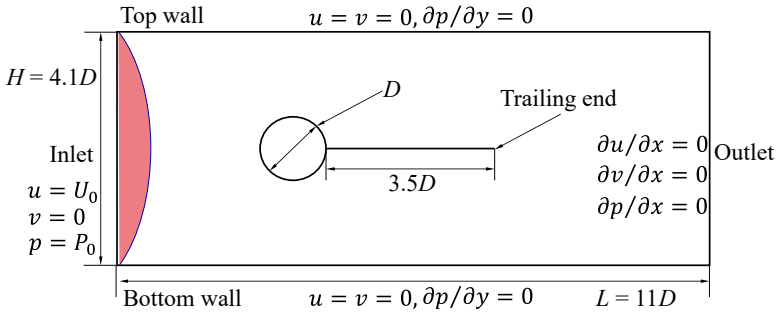

Figure 15: Schematic diagram of flow-induced vibration of a flexible beam behind a stationary cylinder.

2.6.2 Flexible beam behind a stationary cylinder in a channel

Here, a moving boundary case, the FSI of a flexible plate behind a stationary cylinder in a channel, is considered. Fig. 15 shows the schematic diagram of the geometry and the boundary conditions of this case. This case has been used as a benchmark validation for FSI solvers involving large-displacement (Bhardwaj and Mittal, 2012; Lee and You, 2013; Tian et al., 2014a; Wang and Tian, 2019; Zhang et al., 2021).

As shown in Fig. 15, a fixed circular rigid body is submerged in an incompressible fluid. A flexible thin beam is attached downstream to the cylinder. The cylinder has a diameter of D and is centred at the origin. The beam has thickness h and length $L = 3.5D$. A parabolic velocity profile with averaged velocity U_0 and a constant pressure P_0 are imposed at the inlet. No-slip walls are enforced at the top and bottom sides of the computational domain. The normal and shear stress are set to zero at the outlet. The computational domain is a rectangular box ($x \in [-2D, 9D]$ and $y \in [-2.05D, 2.05D]$), and the grid size for the fluid and

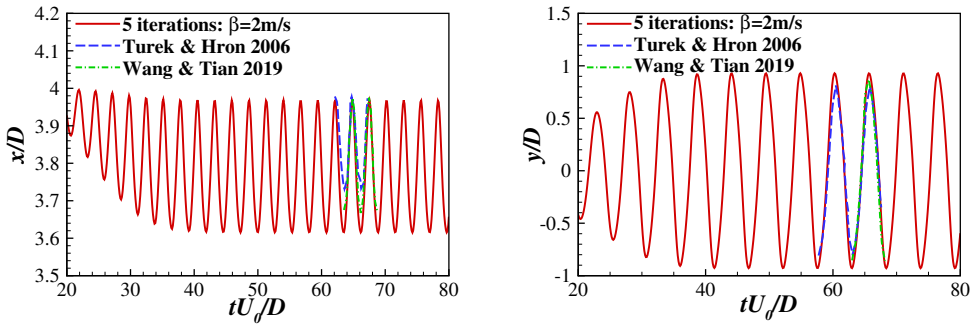

(a) The time history of x-coordinate (b) The time history of y-coordinate

Figure 16: Time histories of the x- and y- coordinate at the trailing end: (a) the time history of x-coordinate, and (b) the time history of y-coordinate. The non-dimensional feedback coefficient $\beta^* = \beta/U_0 = 40$ for $\beta = 2m/s$.

the beam is 0.01D and 0.005D, respectively. The non-dimensional parameters for this case are

$$\mathrm{Re} = \frac{\rho U_0 L}{\mu}, \quad M = \frac{\rho_s}{\rho L}, \quad K_b = \frac{EI}{\rho U_0^2 L^3}, \quad K_s = \frac{Eh}{\rho U_0^2 L}, \tag{33}$$

where ρ_s is the linear density of the beam, M is the structure-to-fluid mass ratio, and K_b and K_s are the bending stiffness and stretching stiffness of the beam, respectively. E is Young's modulus, and $I = h^3/12$ is the moment of inertia of the beam cross-section. Here $Re = 100, M = 2.0$, and $K_b = 1.111$. A large stretching stiffness $K_s = 500$ is chosen to achieve a nearly inextensible beam (Wang and Tian, 2019).

Fig. 16 compares the time histories of the x- and y- coordinate at the trailing end. It shows that the flexible beam reaches a periodic oscillation at around $tU_0/D = 40$. A reasonably good agreement is found between the present results and other numerical results of literature (Bhardwaj and Mittal, 2012; Turek and Hron, 2006; Tian et al., 2014a; Wang and Tian, 2019; Zhang et al., 2021).

Table 2 shows the comparison of the mean drag coefficient $C_{D,m} = F_{D,m}/(0.5\rho U_0^2 D)$ ($F_{D,m}$ is the mean drag of the cylinder-beam system), Strouhal number defined as $St = fD/U_0$ (f is the oscillation frequency), and vertical oscillation amplitude of the trailing end. Overall, the present results show reasonable agreement with previous results.

The Strouhal number St, which characterizes the flapping shedding frequency, is 0.186 in the present Algorithm 3 with 1 iteration and $\beta = 2m/s$ simulation, while that computed by previous studies (Turek and Hron, 2006; Bhardwaj and Mittal, 2012; Wang and Tian, 2019) is 0.19 (a difference of about 2.1%). In present simulation of Algorithm 3 with five iterations and $\beta = 2m/s$, $St = 0.185$ (a difference with previous results of 2.6%), suggesting that the iterations do not affect the prediction of the flapping frequency of the beam. For the 1 iteration with $\beta = 5.2m/s$, the prediction is also not affected. Given that three significant digits of St are kept here, and a thin plate is used instead of the plate of finite thickness, the deviations of the frequency predicted by our simulations are reasonable. This case also shows the capability of this solver in modelling FSI involving a thin flexible plate.

Table 2: Comparison of the mean drag $C_{D,m}$, Strouhal number St, and vertical oscillation amplitude A_m of the beam. Note: $U_0 = 0.05m/s$ is used for all tested cases. Therefore, the non-dimensional feedback coefficient $\beta^* = \beta/U_0 = 40$ for $\beta = 2m/s$, and $\beta^* = 104$ for $\beta = 5.2m/s$.

Sources	$C_{D,m}$	St	A_m
Turek and Hron (2006)	4.13	0.19	0.83
Bhardwaj and Mittal (2012)	3.56	0.19	0.92
Tian et al. (2014a)	4.11	0.19	0.78
Wang and Tian (2019)	4.34	0.19	0.85
Zhang et al. (2021)	–	0.180-0.188	0.86-0.89
Algorithm 3: 1 iteration, $\beta = 2m/s$	3.943	0.186	0.926
Algorithm 3: 5 iterations, $\beta = 2m/s$	3.903	0.185	0.929
Algorithm 3: 1 iteration, $\beta = 5.2m/s$	3.906	0.183	0.933

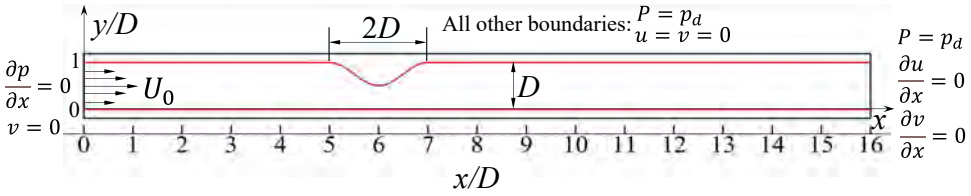

Figure 17: Schematic diagram of fluid flow through a 2-D asymmetric stenosis. All other boundaries: all other computational boundaries except for the inlet and outlet.

2.6.3 Fluid flow through a 2-D asymmetric stenosis

Many studies examined the iteration effects of the IBM in the scenarios of external flows (e.g. flow over a cylinder (Tao et al., 2019a; Zhang et al., 2020)). However, there is no study on the iteration effects of IBM in internal flows. Therefore, the iteration effects of the IBM are tested here for fluid flow through an asymmetric stenosis with a diameter restriction of 50% at the constriction. Fig. 17 shows the schematic diagram of the stenosis, where two red lines represent the upper and lower channel walls. A cosine function dependent on the axial coordinate x is used to describe the upper stenosed channel wall,

$$y(x) = D\left[1 - a_0\left(1 + \cos\left(\frac{2\pi(x - x_0)}{L}\right)\right)\right], \tag{34}$$

where D is the diameter of the non-stenosed channel, $a_0 = 0.25$ for the 50% diameter reduction, $x_0 = 6$ is the x coordinate of the center of the stenosis ($x_0 - L/2 \leq x \leq x_0 + L/2$), and $L = 2D$ is the length of the stenosis. The length and width of the whole computational domain are $16D$ and $1.2D$, respectively. A steady Poiseuille flow with an averaged velocity U_0 is imposed at the upstream inlet, and a constant pressure p_d is specified at the downstream outlet. The grid size for the fluid and the channel wall is $dx = 0.01D$ and $ds = 0.005D$, respectively.

The fluid flow through a 2-D asymmetric stenosis at $Re = 200$ is simulated and is validated against the commercial software ANSYS Fluent. In the ANSYS Fluent, a boundary-fitted grid with a total grid size of 498×100 quadrilateral elements is generated. A steady Poiseuille flow with averaged velocity U_0 imposed at the inlet using the user-defined function (UDF). The flow

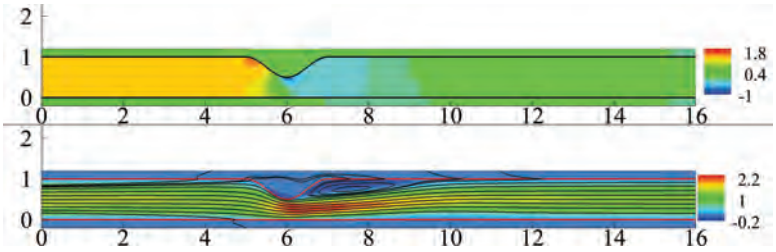

(a) 1 iteration

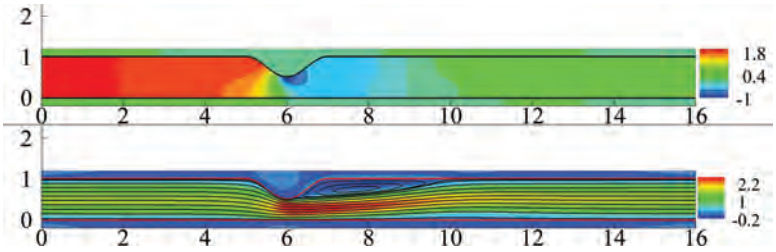

(b) 5 iterations

Figure 18: Pressure and streamwise velocity contours of a 2-D asymmetric stenosis at $tU_0/D = 100$: (a) 1 iteration, and (b) 5 iterations. The velocity is non-dimensionalized by inlet averaged velocity U_0. The pressure here is relative pressure to the outlet pressure p_d and is non-dimensionalized by ρU_0^2. $\beta = 2m/s$ is used for these two cases.

is laminar and steady, which is solved by pressure-velocity coupling scheme. This scheme has the advantage of solving the momentum and pressure correction separately, which simplifies computations but can led to slower convergence for poorly constructed grids(ANSYS, 2009). For the space discretization, a least squares cell based, body force weighted, second order upwind scheme are chosen for the gradient, pressure and momentum, respectively. As the flow is simple (i.e., laminar and steady) and at low Reynolds number $Re = 200$, second order space discretization is enough for resolving all concerned physical quantities such as the pressure and velocity. The convergence standard $\epsilon = 1 \times 10^{-5}$ is chosen.

Fig. 18 shows the simulated pressure and streamwise velocity contours at $tU_0/D = 100$ (the flow reaches a steady state) for 1 iteration (i.e. Algorithm 3 with 1 iteration and $\beta = 2m/s$) and five iterations (i.e. Algorithm 3 with five iterations and $\beta = 2m/s$), respectively. As shown in the pressure contours, a low-pressure area is observed at the posterior part of the stenosis. Compared with the pressure contours for one iteration, a much higher pressure region is observed in the upstream channel of the stenosis for five iterations. The velocity contours show that a stable jet flow is formed downstream of the stenosis. The velocity increases significantly due to the constriction of the upper channel wall. The jet flow is stronger for the five iterations. The streamlines penetrate through the upper and lower channel walls in the velocity contours for one iteration, but not for five iterations.

These observations again demonstrate that the iterative IBM can suppress the spurious flow penetration and improve the no-penetration boundary conditions at the walls. As a result, the mass conservation in the channel is more strictly satisfied, which is crucially important for simulating internal flows.

Fig. 19 shows the velocity profiles at four different axial positions at $x = 5.85$ and $x = 7$. As shown in Fig. 19, the velocity profiles predicted by the present 5 iterations and 1 iteration

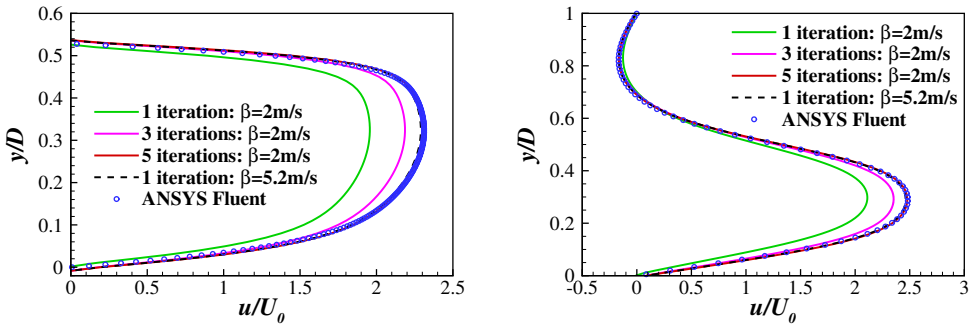

(a) At $x = 5.85$ (b) At $x = 7$

Figure 19: Velocity profiles at $tU_0/D = 100$ when the flows are steady: (a) $x = 5.85$, and (b) $x = 7$. Note: $U_0 = 0.05m/s$ is used for all tested cases. Therefore, the non-dimensional feedback coefficient $\beta^* = \beta/U_0 = 40$ for $\beta = 2m/s$, and $\beta^* = 104$ for $\beta = 5.2m/s$.

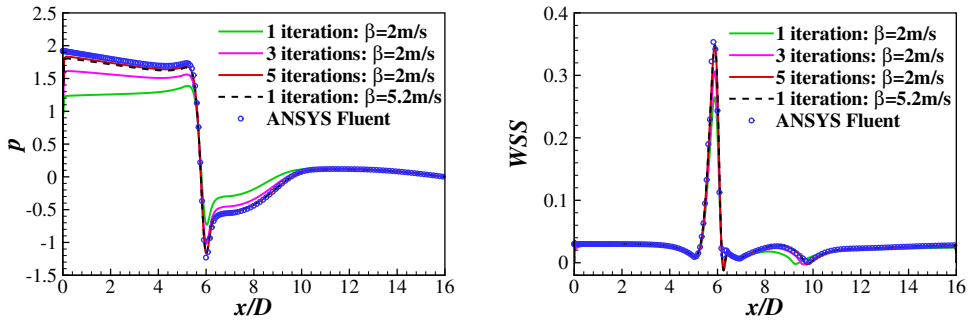

(a) Pressure along the upper channel wall (b) WSS along the upper channel wall

Figure 20: Pressure and wall shear stress (WSS) along the upper channel wall at $tU_0/D = 100$: (a) Pressure, and (b) WSS. The pressure here is relative pressure to the outlet pressure p_d. The pressure and WSS are non-dimensionalized by ρU_0^2. Note: $U_0 = 0.05m/s$ is used for all tested cases. Therefore, the non-dimensional feedback coefficient $\beta^* = \beta/U_0 = 40$ for $\beta = 2m/s$, and $\beta^* = 104$ for $\beta = 5.2m/s$.

with $\beta = 5.2m/s$ agree very well at all the axial positions with the numerical solutions of the commercial software ANSYS Fluent. In comparison, big discrepancies are observed at all the axial positions for the present 1 iteration with $\beta = 2m/s$. Small discrepancies are observed at all axial positions for the present 3 iterations with $\beta = 2m/s$. The under-prediction of velocity for the 1 iteration and 3 iterations with $\beta = 2m/s$ is due to fluid leakage from the channel as a result of spurious flow penetration.

The pressure and wall shear stress (WSS) on the arterial wall are of great interest to the medical community as they play an essential role in the genesis and progression of cardiovascular diseases (Malek et al., 1999; Huang et al., 2021a). Therefore, the distributions of pressure and WSS along the upper channel wall are shown in Fig. 20. The pressure and WSS are linearly interpolated based on the corresponding values at 2.5 and 5.0 grid points inward of the channel walls (Huang et al., 2020, 2021b). Results of 1 iteration with $\beta = 2m/s$ largely under-predict the pressure and WSS because the no-slip and no-penetration boundary conditions at the channel walls are not exactly satisfied. This issue can be well addressed by 5

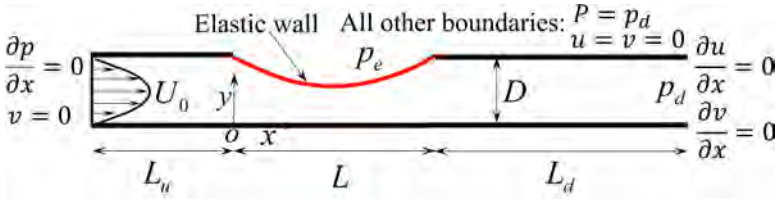

Figure 21: Schematic diagram of one-sided collapsible channel flow. All other boundaries: all other computational boundaries except for the inlet and outlet.

iterations or using $\beta = 5.2m/s$ of the IBM. Small discrepancies are observed for 3 iterations. The iteration allows for local flow reconstruction in the vicinity of the channel walls (Huang et al., 2021b) and the results agree very well with those of ANSYS. Thus, the observations suggest that the iteration and $\beta = 5.2m/s$ both improve the enforcement of the no-slip and no-penetration boundary conditions on the channel walls.

2.6.4 One-sided collapsible channel flow

Here, the iteration effects of the IBM are examined for an internal flow with a moving and deformable boundary by considering a 2-D incompressible flow in a one-sided collapsible channel. As shown in Fig. 21, a part of the channel wall is replaced by an elastic beam. The elastic beam has length L and is subjected to an external pressure p_e. The rigid channel has a width of D. A steady Poiseuille flow with averaged velocity U_0 is imposed at the upstream inlet, and a constant pressure p_d is specified at the downstream outlet.

The averaged flow velocity at the inlet U_0, channel height D, and fluid density ρ are used to non-dimensionalize this system, giving five non-dimensional parameters: the Reynolds number, the structure-to-fluid mass ratio, the stretching stiffness, the bending stiffness and the external pressure, which are respectively given by

$$Re = \frac{U_0 D}{\nu}, M = \frac{\rho_s}{\rho D}, K_s = \frac{Eh}{\rho U_0^2 D}, K_b = \frac{EI}{\rho U_0^2 D^3}, P_e = \frac{p_e - p_d}{\rho U_0^2}. \tag{35}$$

Here $Re = 250$, $M = 1$, $K_s = 56.88$ and $P_e = 1.95$ are used. A no-slip boundary condition is applied along the channel wall, including the elastic segment. Clamped conditions are used at the two ends of the elastic wall. The remaining parameters are $L_u = 5D$, $L_d = 30D$, $L = 5D$, and $K_b/K_s = (h^2/12D^2) \approx 10^{-5}$ for a wall thickness h of 1% of the channel height. The nonlinear dynamics of the collapsible channel wall is treated as a Bernoulli-Euler beam with zero initial tension and solved by the finite difference method. The grid size for the fluid and the channel walls is $0.01D$ and $0.005D$, respectively. More computational details can be found in our previous work (Huang et al., 2020, 2021b,c,b). Here the iteration effects of the IBM are examined by considering five cases: 1 iteration, 3 iterations, 5 iterations, dynamic iterations with $\beta = 2m/s$ and 1 iteration with $\beta = 5.2m/s$. For the dynamic iterations, the iteration is terminated when the maximum velocity error at the immersed boundary is less than a pre-set criterion (i.e. $max(U_{error}(s,t)) \leq 5 \times 10^{-3}$) (Huang et al., 2021b),

$$U_{error}(s,t) = \frac{\sqrt{(\boldsymbol{U}_{ib}^m(s,t) - \boldsymbol{U}(s,t))^2}}{U_0}. \tag{36}$$

For the dynamic iterations with $\beta = 2m/s$, the average iteration number is 6.17. The iteration number is reduced to 1 or 2 using $\beta = 5.2m/s$.

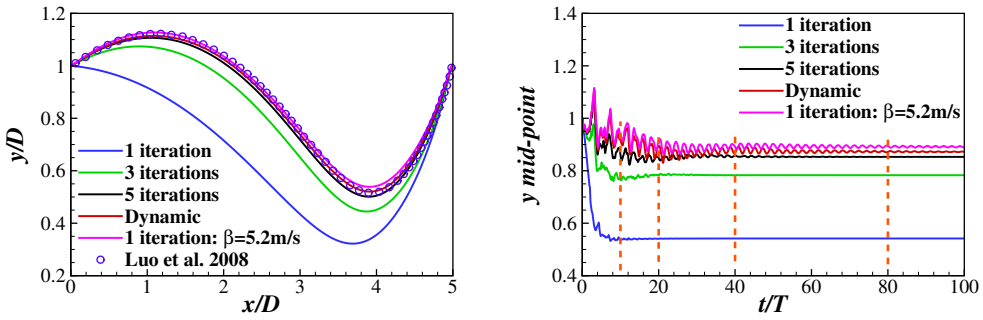

(a) Wall shapes at $t/T = 100$ (b) Time history of middle point

Figure 22: Deformation of one-sided collapsible channel flow: (a) comparison of wall shapes from present IB-LBM with the ALE (arbitrary Lagrangian Eulerian) of Luo et al. (2008); (b) the time history of the y-coordinate for the mid-point ($x = 2.5$ initially) on the upper elastic wall for different iteration strategies: 1 iteration, 3 iterations, 5 iterations, dynamic iterations with $\beta = 2m/s$ and 1 iteration with $\beta = 5.2m/s$. $T = D/U_0$ is the reference time. Note: $U_0 = 0.05m/s$ is used for all tested cases. The non-dimensional feedback coefficient $\beta^* = \beta/U_0 = 40$ for $\beta = 2m/s$, and $\beta^* = 104$ for $\beta = 5.2m/s$.

Fig. 22(a) shows the comparison of wall shapes from present simulations with the ALE of Luo et al. (2008). The simulations with dynamic iterations and 1 iteration with $\beta = 5.2m/s$ predict the most accurate wall shape while the 1 iteration with $\beta = 2m/s$ predicts the worst. The prediction improves as the increase of iteration. Fig. 22(b) shows the time history of the y-coordinate of the mid-point of the upper elastic wall for different iterations. It shows that the time histories of the y-coordinate are quite different not only in the final value but also in the oscillation trajectory. For the dynamic iterations and 1 iteration with $\beta = 5.2m/s$, the oscillations are evident during the transition state ($0 \leq t/T \leq 50$) while the oscillation amplitude is gradually damped out as time increases. For the other three cases (i.e. 1 iteration, 3 iterations and 5 iterations, the elastic walls are in a steady state for most of the time. The different stabilities predicted by these five iteration strategies are due to the boundary velocity slip error and the spurious flow penetration on the elastic walls for the 1 iteration, 3 iterations and 5 iterations. The boundary velocity slip error and the spurious flow penetration on the elastic wall are demonstrated respectively in Figs. 23 and 24.

In order to examine the boundary velocity slip error, the velocity error along the elastic wall, as shown in Fig. 23, is calculated at $t/T = 80$. It shows that the maximum velocity error is on the collapsible part of the wall ($x/D \approx 1.4$) for all the iteration strategies. Please note that the pressure inside the channel is generally lower than the external pressure. For the 1 iteration case, a lower β induces a larger velocity error which in turn reduces the pressure drop and consequently increases the pressure difference (see Fig. 24(a)), leading to a larger collapse deformation. A larger collapse deformation increases the velocity near the collapsed region leads to a lower pressure enlarging the pressure difference. As discussed in Appendix A, the physical meaning of the Lagrangian force is to balance the fluid force which is the pressure difference here. Therefore, according to $\Delta p^* \approx \rho\beta\Delta U^*$ (where Δp^* is the dimensionless pressure difference), a larger Δp^* leading to a larger velocity error, as observed in Fig. 23. In addition, the velocity error profile is similar to the distribution of pressure (not shown for this case but the distribution is close to that shown in Fig. 20(a)).

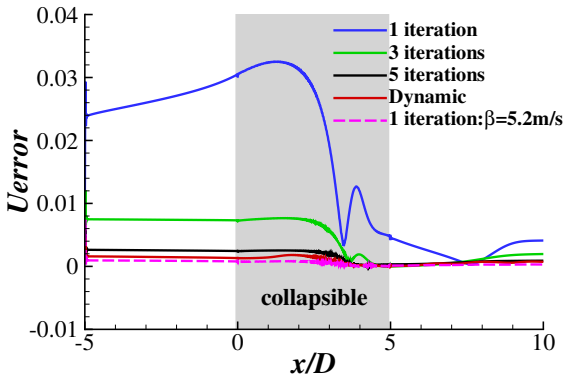

Figure 23: Velocity error U_{error} distributions on the upper channel wall (only for $-5 \leq x/D \leq 10$) at t/T=80 as indicated in Fig. 22(b). The collapsible segment of the upper channel wall is highlighted by a grey shaded area. Note: Due to the velocity error scales with the Courant number (C=$U_0\Delta t/\Delta x$) (Gsell and Favier, 2021), $U_0 = 0.05m/s$ is used for all tested cases. Therefore, the non-dimensional feedback coefficient $\beta^* = \beta/U_0 = 40$ for $\beta = 2m/s$, and $\beta^* = 104$ for $\beta = 5.2m/s$.

Serious boundary velocity slip error is on the channel wall from the inlet to the end of the elastic wall, and this error can be significantly (more than an order of magnitude) reduced by five iterations or 1 iteration with $\beta = 5.2m/s$. For the 1 iteration with $\beta = 5.2m/s$, the overall velocity error is the smallest (averaged $U_{error} \approx 0.0001$) among all the five iteration strategies. The observations also suggest that either iterations or a larger feedback coefficient can reduce the velocity slip error on the solid wall.

Fig. 24 shows the pressure and velocity contours of the 1 iteration and the dynamic iterations, respectively. As shown in the pressure contours, a high-pressure region is developed upstream of the constriction, and a low-pressure region is observed downstream of the elastic wall. Compared with the pressure contours for the one iteration, a much higher pressure region is observed at the upstream of the constriction for the dynamic iterations, causing the upstream half of the elastic wall to bulge out. A jet flow is developed downstream of the constriction, as shown in the velocity contours. For the dynamic iterations, the high-velocity region at the constriction is more prominent and higher than that of the 1 iteration, indicating a stronger jet flow. For the 1 iteration, the streamlines penetrate through the upper and lower channel walls while no streamline penetrates through the channel walls for the dynamic iterations. Severe streamline penetrations at the upstream elastic wall are observed, and the spurious flow penetrations are less severe downstream of the constriction, especially at $x/D > 17$. The 1 iteration predicts a larger recirculation area due to the narrower constriction of the channel.

2.6.5 Three-dimensional collapsible tube flow

Here, the computation of a steady flow in a collapsible tube is conducted to examine the iteration effects of the IBM. The coupled nonlinear system for the FSIs in the collapsible tube is solved by the finite element-immersed boundary-lattice Boltzmann method (FE-IB-LBM) FSIs solver. D3Q19 model has been proven to be accurate enough for low to medium Reynolds number flows(Xu et al., 2018; Ma et al., 2020), and MRT has been proven to be a numerically

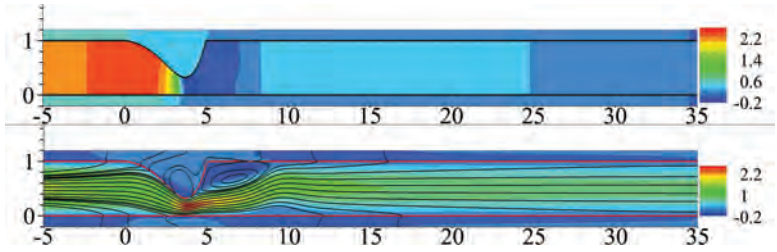

(a) 1 iteration

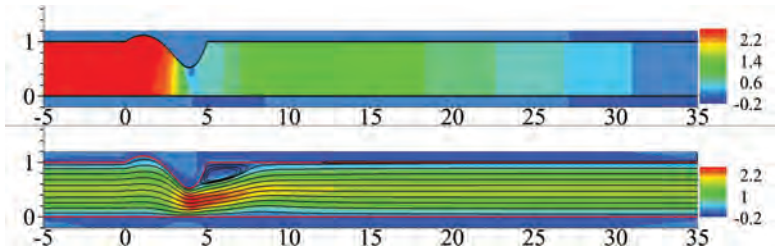

(b) Dynamic iterations

Figure 24: Instantaneous pressure and velocity contours at $t/T = 100$: (a) 1 iteration, and (b) dynamic iterations. $\beta = 2m/s$ is used for these two cases. Note: the aspect ratio (length/width) is set to 0.3 for an overview of the whole flow field.

stable model(Lallemand and Luo, 2000; Krüger et al., 2017). Therefore, the D3Q19 LBM with MRT model is adopted for the fluid dynamics.. The structural equation is solved by an explicit FEM. The strain of the wall is assumed to be small which enables the tube wall to be treated as a linear elastic structure. The dynamics for the solid is

$$\rho_m \frac{d^2 \boldsymbol{u}_s}{dt^2} + c\frac{d\boldsymbol{u}_s}{dt} - \nabla \cdot \boldsymbol{\sigma} - \rho_m \boldsymbol{b} = 0, \tag{37}$$

where ρ_m is the solid density, $\boldsymbol{u}_s(\boldsymbol{X}, t)$ denotes the solid displacement field, c is the material damping, $\boldsymbol{\sigma}$ is the Cauchy stress tensor and $\boldsymbol{b}$ is the body force.

A 3D incompressible flow in a thin-walled collapsible tube of undeformed radius R, length L and wall thickness h is considered. As illustrated by Fig. 25, the elastic wall is subjected to an external pressure p_e, and the tube wall material has Young's modulus E and Poisson ratio ν_s. The rigid tube has a diameter of D. The averaged flow velocity at the inlet U_0, tube diameter D and fluid density ρ are used to non-dimensionalize this system, giving four non-dimensional parameters governing this FSI system: the Reynolds number, structure-to-fluid mass ratio, bending stiffness and external pressure are given respectively by

$$Re = \frac{U_0 D}{\nu}, \quad M = \frac{\rho_m h}{\rho D}, \quad K_b = \frac{Eh^3}{12\left(1-\nu_s^2\right)\rho U_0^2 D^3}, \quad P_e = \frac{p_e - p_d}{\rho U_0^2}. \tag{38}$$

A no-slip boundary condition is applied along the tube wall. The tube is clamped at both ends and is discretized with 26400 isoparametric 3D solid elements (20 nodes for each element and one element in the thickness direction), giving 185460 nodal points with three degrees of freedom (displacements) for each structural element. A steady Hagen-Poiseuille velocity profile with average velocity U_0 is imposed at the inlet, and a constant pressure $p_d = 0$ is specified at the downstream outlet. The initial flow field is initialized as:

$$\frac{u}{U_0} = 0, \quad \frac{v}{U_0} = 0, \quad \frac{w}{U_0} = 2\left(1 - r^2\right), \tag{39}$$

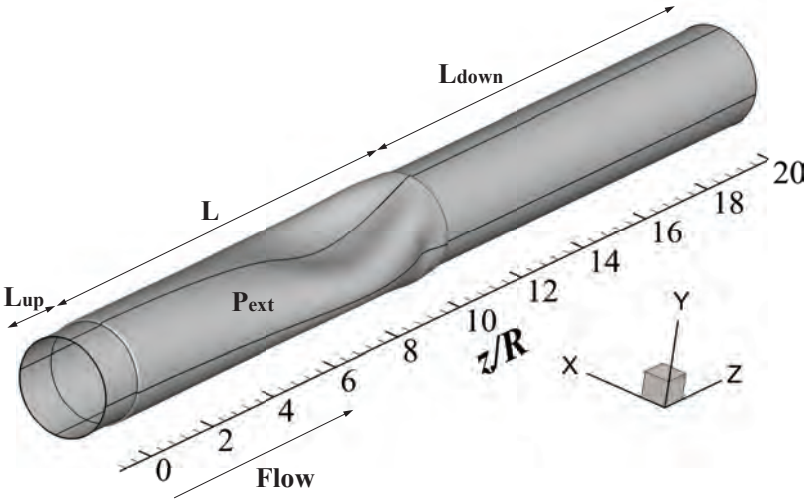

Figure 25: Schematic diagram of fluid flow through a collapsible tube.

where u, v and w are the velocity in $x-$, $y-$ and $z-$directions, respectively, and $r = \sqrt{y^2 + x^2}$ is the radial distance from the tube center-line.

The axisymmetric solution is remarkably robust, such that a perturbation load is required in order to force the structure collapse into a mode-2 (two-lobed shape) buckling. A perturbation is initially added to the external pressure as in Marzo et al. (2005)

$$p_{load} = a_0 + a_1 X^2, \tag{40}$$

where X is the horizontal spatial coordinate of the tube as shown in Fig. 25, and the coefficients a_0 and a_1 are

$$a_0 = p_e + C, \quad a_1 = -\frac{C}{(R+h)^2}, \tag{41}$$

where C is the parameter controlling the degree of perturbation and is chosen as $0.1p_e$. p_{load} was set to zero once the tube had buckled.

The computation parameters are $R = 0.5m$, $L_u = R = 0.5m$, $L = L_d = 10R = 5m$, $\nu_s = 0.49$, $E = 4559.4Pa$, $h = 0.05R = 0.025m$ and $\rho_m = 1000kg/m^3$, giving the same nondimensional parameters used by Hazel and Heil (2003): $Re = 128$, $M = 25$, $K_b = 0.030517$, $P_e = 5.46875$. To approximate the steady flow, an empirical damping ratio $\zeta = c/c_c = 0.05$ ($c_c = 2\sqrt{Km}$ is the critical damping, $K = E(h/R)^3/12\,(1-\nu_s^2)$ is the bending modulus and m is the mass of the elastic tube) is used here to damp out the oscillations. More computational details can be found in our previous publications (Huang, 2021; Huang et al., 2021c).

Fig. 26 shows the comparison of present computations with those of Hazel and Heil (2003) and Zhang et al. (2018). The simulation with dynamic iterations and 1 iteration with $\beta = 5.2m/s$ predicts the most accurate wall shape while the 1 iteration with $\beta = 2m/s$ predicts the worst. This observation suggest again that either iterations or a larger feedback coefficient can improve the no-slip and no-penetration boundary conditions at the fluid-solid interface.

2.6.6 Discussions

The non-iterative IBMs with and without the prediction step (Algorithm 1 and 2) and the iterative IBM (Algorithm 3) are examined for external (i.e. flow over a stationary cylinder

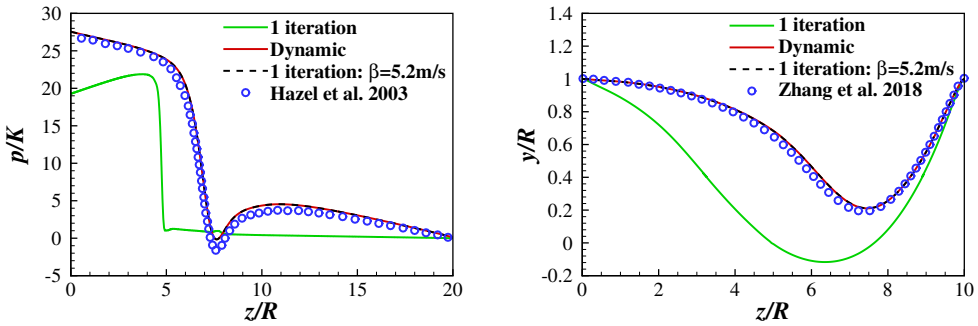

(a) Pressure distribution along the tube centreline

(b) Wall shape of the tube projected to the symmetry plane (Y-Z plane)

Figure 26: Comparison of steady solutions between present IB-LBM computations and FEM computations of Hazel and Heil (2003) and Zhang et al. (2018): (a) pressure distribution along the tube centreline, and (b) wall shape of the tube projected to the symmetry plane. The coordinates (x, y, z) are scaled to the radius R and the pressure is scaled to the bending modulus K of the tube, as in Hazel and Heil (2003). For 1 iteration and dynamic iterations, $\beta = 2m/s$. Note: $U_0 = 0.05m/s$ is used for all tested cases. Therefore, the non-dimensional feedback coefficient $\beta^* = \beta/U_0 = 40$ for $\beta = 2m/s$, and $\beta^* = 104$ for $\beta = 5.2m/s$.

and flow-induced vibration of a flexible beam attached behind a cylinder) and internal (flow through a 2-D asymmetric stenosis, a one-sided collapsible channel, and a 3-D collapsible tube) flows. Compared with Algorithm 1, the velocity prediction step in Algorithm 2 and Algorithm 3 can help to suppress the spurious flow penetration and reduce the velocity slip on the immersed boundaries. The velocity error that occurred in the 1 iteration feedback IBM with the conventional feedback coefficient $\beta = 2m/s$ is of low consequence for external flows as it does not introduce significant deviation in predicting the forces on the structure and the structure deformation. However, it matters for internal flows, as it leads to significant deviation in the force prediction and the structure deformation. In addition, Luo et al. (2007) showed that reducing the velocity error is also quite important in the multiphase flow simulation (e.g. particle-laden flows).

For external flows, the velocity error on the cylinder does not cause significant deviation in the pressure and shear force on the solid. Therefore, the errors in predicting the drag coefficient C_D and the structure deformation are small. While for flows in a 2-D asymmetric stenosis, as shown in Fig. 20(a), the velocity error could cause a large maximum pressure error (35.94% for the case considered here) at the inlet. The boundary velocity slip causes a maximum WSS error of 25.04% at the most constriction region of the upper channel wall (Fig. 20(b)). Therefore, for internal flows with flexible channel walls, such as the one-sided collapsible channel flow and the 3-D collapsible tube flow considered here, the significant velocity error (Fig. 23) on the channel walls causes a significant error in the pressure and shear force. As a result, the error in the force prediction causes a significant error in the wall deformation (Fig. 22), which in turn enlarges the error in velocity.

Results have shown that the iterative IBM or the non-iterative IBM with a larger feedback coefficient can suppress the boundary velocity-slip error and spurious flow penetration on the solid wall. As a result, good force production and structure deformation are achieved. The iteration number and the computational time can be significantly reduced by amplifying the

feedback coefficient β. The iterative IBM and the method of amplifying the feedback coefficient could effectively suppress boundary slip and spurious flow penetration. Overall, this strategy is highly effective and efficient and effortless without any extra effort. Based on our extensive testing, $\beta = 5.2m/s$ can cause serious numerical instabilities in the cases of low mass ratio and large stretching stiffness, while the iterative IBM with $\beta = 2m/s$ works well in this case and are thus more numerically stable. It should be noted that the optimal feedback coefficient will be a bit different for different flow solvers/methods, for example, different force schemes in the LBM or different delta functions (Huang and Tian, 2019). On the other hand, the three algorithms presented in this study are diffused-interface IBMs, which requires further effort in order to be applied to high Reynolds number flows (Mittal and Bhardwaj, 2022).

Just as pointed out by Zhao et al. (2021), the boundary condition-enforced IB-LBM Wu and Shu (2010); Chen et al. (2020b) can accurately fulfill the no-slip boundary condition but it is quite computational challenge when simulating moving boundary problems as a large matrix must be assembled and implicitly resolved at every time step. The feedback IBM (Algorithm 3) presented in our manuscript is an explicit method, in which calculations of the large matrix is avoid and no-slip and no-penetration boundary conditions are well fulfilled either by small feedback coefficient with several iterations (e.g., 5 iterations with $\beta = 2m/s$) or the optimal feedback coefficient with only 1 iteration (e.g., 1 iteration with $\beta = 5.2m/s$). Compared with the explicit technique-based IB-LBM proposed by Zhao et al. (2021), the feedback IB-LBM (Algorithm 3) presented in our manuscript has an adjustable feedback coefficient β, which is very attractive for complex fluid-structure interaction problems involving large and elastic deformation, large amplitude vibration, low structure-to-fluid mass ratio and turbulent flows. For example, for numerical instabilities often encountered in low structure-to-fluid mass ratio cases, the numerical stability can be improved by a small feedback coefficient, and the boundary slip and spurious flow penetration can be suppressed by several iterations (e.g., 5 iterations with $\beta = 2m/s$).

2.7 Conclusions

The performance of three implementations of the feedback IBM has been studied. The streamline penetration, velocity error on the immersed boundary and consequences in the force production and structure deformation are discussed by simulating external (a uniform flow over a cylinder, flow-induced vibration of a flexible beam attached behind a cylinder) and internal flows (flow through a 2-D asymmetric stenosis, a one-sided collapsible channel and a 3-D collapsible tube). Results show that the widely reported streamline penetration can be significantly reduced by properly implementing the feedback IBM or employing the iterative IBM. The boundary velocity error does not significantly affect the force production and structure deformation for external flows. However, for internal flows such as the stenosis and the collapsible channel/tube flows, reducing the velocity error by using the iterative IBM or the optimal feedback coefficient substantially improves the prediction of the force distribution and structure deformation. Moreover, the value of the feedback coefficients could be smaller for the iterative IBM, which is very attractive for improving the numerical stability for low structure-to-fluid mass ratio cases but at the expense of more iterations. The results obtained provide an important guideline for the correct use of the feedback IBMs.

References

Acharya, M., Metwally, M.H., 1992. Unsteady pressure field and vorticity production over a pitching airfoil. AIAA Journal 30, 403–411. doi:10.2514/3.10931.

ANSYS, 2009. Fluent theory guide. Release 12.0, help system, ANSYS, Inc. 10, 72.

Berthelsen, P.A., Faltinsen, O.M., 2008. A local directional ghost cell approach for incompressible viscous flow problems with irregular boundaries. J. Comput. Phys. 227, 4354–4397.

Bhardwaj, R., Mittal, R., 2012. Benchmarking a coupled immersed-boundary-finite-element solver for large-scale flow-induced deformation. AIAA Journal 50, 1638–1642.

Bhat, S.S., Govardhan, R.N., 2013. Stall flutter of NACA 0012 airfoil at low Reynolds numbers. Journal of Fluids and Structures 41, 166–174. doi:10.1016/j.jfluidstructs.2013.04.001.

Bhat, S.S., Zhao, J., Sheridan, J., Hourigan, K., Thompson, M.C., 2018. The leading-edge vortex on a rotating wing changes markedly beyond a certain central body size. Royal Society Open Science 5, 172197. doi:10.1098/rsos.172197.

Bhat, S.S., Zhao, J., Sheridan, J., Hourigan, K., Thompson, M.C., 2019a. Aspect ratio studies on insect wings. Physics of Fluids 31, 121301. doi:10.1063/1.5129191.

Bhat, S.S., Zhao, J., Sheridan, J., Hourigan, K., Thompson, M.C., 2019b. Uncoupling the effects of aspect ratio, Reynolds number and Rossby number on a rotating insect-wing planform. Journal of Fluid Mechanics 859, 921–948. doi:10.1017/jfm.2018.833.

Birch, J.M., Dickson, W.B., Dickinson, M.H., 2004. Force production and flow structure of the leading edge vortex on flapping wings at high and low reynolds numbers. Journal of Experimental Biology 207, 1063–1072.

Borazjani, I., Sotiropoulos, F., 2008. Numerical investigation of the hydrodynamics of carangiform swimming in the transitional and inertial flow regimes. J. Exp. Biol. 211, 1541–1558.

Cai, Y., Li, S., Lu, J., 2018. An improved immersed boundary-lattice Boltzmann method based on force correction technique. Int. J. Numer. Methods Fluids 87, 109–133.

Canuto, D., Taira, K., 2015. Two-dimensional compressible viscous flow around a circular cylinder. J. Fluid Mech. 785, 349–371.

Chen, L., Wu, J., Zhou, C., Hsu, S.J., Cheng, B., 2018. Unsteady aerodynamics of a pitching-flapping-perturbed revolving wing at low reynolds number. Physics of Fluids 30, 051903. doi:10.1063/1.5024925.

Chen, L., Zhou, C., Wu, J., 2020a. The role of effective angle of attack in hovering pitching-flapping-perturbed revolving wings at low reynolds number. Physics of Fluids 32, 011906. doi:10.1063/1.5130959.

Chen, Z., Shu, C., Yang, L., Zhao, X., Liu, N., 2020b. Immersed boundary–simplified thermal lattice boltzmann method for incompressible thermal flows. Phys. Fluids 32, 013605.

Cheylan, I., Favier, J., Sagaut, P., 2021. Immersed boundary conditions for moving objects in turbulent flows with the lattice-Boltzmann method. Phys. Fluids 33, 095101.

Connell, B.S.H., Yue, D.K.P., 2007. Flapping dynamics of a flag in a uniform stream. J. Fluid Mech. 581, 33–67.

Corke, T.C., Thomas, F.O., 2015. Dynamic stall in pitching airfoils: Aerodynamic damping and compressibility effects. Annual Review of Fluid Mechanics 47, 479–505. doi:10.1146/annurev-fluid-010814-013632.

Coutanceau, M., Bouard, R., 1977. Experimental determination of the main features of the viscous flow in the wake of a circular cylinder in uniform translation. part 1. steady flow. Journal of Fluid Mechanics 79, 231–256.

Dickinson, M.H., Lehmann, F.O., Sane, S.P., 1999. Wing rotation and the aerodynamic basis of insect flight. Science 284, 1954–1960. doi:10.1126/science.284.5422.1954.

Dupuis, A., Chatelain, P., Koumoutsakos, P., 2008. An immersed boundary–lattice-Boltzmann method for the simulation of the flow past an impulsively started cylinder. J. Comput. Phys. 227, 4486–4498.

Ellington, C.P., van den Berg, C., Willmott, A.P., Thomas, A.L.R., 1996. Leading-edge vortices in insect flight. Nature 384, 626–630. doi:10.1038/384626a0.

Ennos, A.R., 1989. Inertial and aerodynamic torques on the wings of diptera in flight. J. Exp. Biol. 142, 87–95.

Fadlun, E., Verzicco, R., Orlandi, P., Mohd-Yusof, J., 2000. Combined immersed-boundary finite-difference methods for three-dimensional complex flow simulations. J. Comput. Phys. 161, 35–60.

Feng, Z.G., Michaelides, E.E., 2004. The immersed boundary-lattice Boltzmann method for solving fluid–particles interaction problems. J. Comput. Phys. 195, 602–628.

Feng, Z.G., Michaelides, E.E., 2005. Proteus: a direct forcing method in the simulations of particulate flows. Journal of Computational Physics 202, 20–51.

Goldstein, D., Handler, R., Sirovich, L., 1993. Modeling a no-slip flow boundary with an external force field. Journal of Computational Physics 105, 354–366. doi:10.1006/jcph.1993.1081.

Gsell, S., Favier, J., 2021. Direct-forcing immersed-boundary method: A simple correction preventing boundary slip error. J. Comput. Phys. 435, 110265.

Guo, Z.L., Zheng, C.G., Shi, B.C., 2002. Non-equilibrium extrapolation method for velocity and pressure boundary conditions in the lattice Boltzmann method. Chinese physics 11, 366–374.

Han, J.S., Kim, J.K., Chang, J.W., Han, J.H., 2015. An improved quasi-steady aerodynamic model for insect wings that considers movement of the center of pressure. Bioinspiration & Biomimetics 10, 1–14. doi:10.1088/1748-3190/10/4/046014.

Harbig, R.R., Sheridan, J., Thompson, M.C., 2013. Reynolds number and aspect ratio effects on the leading-edge vortex for rotating insect wing planforms. Journal of Fluid Mechanics 717, 166–192. doi:10.1017/jfm.2012.565.

Hazel, A.L., Heil, M., 2003. Steady finite-Reynolds-number flows in three-dimensional collapsible tubes. J. Fluid Mech. 486, 79–103.

He, S., Yang, Z., Sotiropoulos, F., Shen, L., 2021. Numerical simulation of interaction between multiphase flows and thin flexible structures. J. Comput. Phys. , 110691.

Huang, Q., 2021. Low Reynolds number turbulent FSI and its applications in biological flows. Ph.D. thesis. University of New South Wales.

Huang, Q., Mazharmanesh, S., Tian, F.B., Young, J., Lai, J.C.S., Ravi, S., 2021a. CFD solver validations for simulating passively pitching tandem wings in hovering flight, in: MODSIM2021, pp. 71–77.

Huang, Q., Sun, J., Xu, C., 2021a. Effects of waveform shape of pulsatile blood flow on hemodynamics in an artery bifurcation model. Proc. Inst. Mech. Eng. C: J. Mech. Eng. Sci. 235, 428–440.

Huang, Q., Tian, F.B., Young, J., Lai, J.C.S., 2020. A diffused interface immersed boundary–lattice Boltzmann method for simulation of channel flow. AFMC2020, 7-10 December 2020, Brisbane, Australia .

Huang, Q., Tian, F.B., Young, J., Lai, J.C.S., 2021b. Transition to chaos in a two-sided collapsible channel flow. J. Fluid Mech. 926.

Huang, Q., Wang, L., Ravi, S., Tian, F.B., Young, J., Lai, J.C.S., 2021c. Benchmarking a coupled finite element–immersed boundary–lattice Boltzmann method solver for simulations of collapsible tube flows, in: ACCM2021, p. 15.

Huang, Q., Wang, L., Tian, F.B., Young, J., Lai, J.C.S., 2021b. A diffused interface immersed boundary–lattice Boltzmann method for simulation of stenosis. 14th WCCM & ECCOMAS Congress .

Huang, W.X., Sung, H.J., 2009. An immersed boundary method for fluid–flexible structure interaction. Comput. Methods Appl. Mech. Eng. 198, 2650–2661.

Huang, W.X., Tian, F.B., 2019. Recent trends and progress in the immersed boundary method. Proceedings of the Institution of Mechanical Engineers, Part C: Journal of Mechanical Engineering Science 233.

Hunt, J.C.R., Wray, A.A., Moin, P., 1988. Eddies, streams, and convergence zones in turbulent flows, in: Center for Turbulence Research Report CTR-S88, pp. 193–208.

Jardin, T., 2017. Coriolis effect and the attachment of the leading edge vortex. Journal of Fluid Mechanics 820, 312–340. doi:10.1017/jfm.2017.222.

Ji, C., Munjiza, A., Williams, J., 2012. A novel iterative direct-forcing immersed boundary method and its finite volume applications. J. Comput. Phys. 231, 1797–1821.

Jiang, M., Liu, Z., 2019. A boundary thickening-based direct forcing immersed boundary method for fully resolved simulation of particle-laden flows. J. Comput. Phys. 390, 203–231.

Kang, S.K., Hassan, Y.A., 2011. A comparative study of direct-forcing immersed boundary-lattice Boltzmann methods for stationary complex boundaries. Int. J. Numer. Meth. Fluids 66, 1132–1158.

Karakas, F., Fenercioglu, I., 2016. Effect of side-walls on flapping-wing power-generation: an experimental study. Journal of Applied Fluid Mechanics 9, 2769–2779. doi:10.29252/jafm.09.06.25997.

Kim, Y., Peskin, C.S., 2007. Penalty immersed boundary method for an elastic boundary with mass. Phys. Fluids 19, 053103.

Krüger, T., Kusumaatmaja, H., Kuzmin, A., Shardt, O., Silva, G., Viggen, E.M., 2017. The lattice boltzmann method. Springer International Publishing 10, 4–15.

Krüger, T., Varnik, F., Raabe, D., 2011. Efficient and accurate simulations of deformable particles immersed in a fluid using a combined immersed boundary lattice Boltzmann finite element method. Comput. Math. Appl. 61, 3485–3505.

Kruyt, J.W., van Heijst, G.F., Altshuler, D.L., Lentink, D., 2015. Power reduction and the radial limit of stall delay in revolving wings of different aspect ratio. Journal of the Royal Society Interface 12, 20150051.

Lallemand, P., Luo, L.S., 2000. Theory of the lattice Boltzmann method: Dispersion, dissipation, isotropy, Galilean invariance, and stability. Physical Review E - Statistical Physics, Plasmas, Fluids, and Related Interdisciplinary Topics 61, 6546–6562.

Lee, J., You, D., 2013. Study of vortex-shedding-induced vibration of a flexible splitter plate behind a cylinder. Phys. Fluids 25, 110811.

Lee, Y.J., Lua, K.B., Lim, T.T., Yeo, K.S., 2016. A quasi-steady aerodynamic model for flapping flight with improved adaptability. Bioinspiration & Biomimetics 11, 36005. doi:10.1088/1748-3190/11/3/036005.

Lentink, D., Dickinson, M.H., 2009. Rotational accelerations stabilize leading edge vortices on revolving fly wings. Journal of Experimental Biology 212, 2705–2719. doi:10.1242/jeb.022269.

Lentink, D., Dickson, W.B., Van Leeuwen, J.L., Dickinson, M.H., 2009. Leading-edge vortices elevate lift of autorotating plant seeds. Science 324, 1438–1440.

Linnick, M.N., Fasel, H.F., 2005. A high-order immersed interface method for simulating unsteady incompressible flows on irregular domains. J. Comput. Phys. 204, 157–192.

Liu, Z., Tian, F.B., Young, J., Lai, J.C.S., 2017. Flapping foil power generator performance enhanced with a spring-connected tail. Phys. Fluids 29, 123601.

Luo, H., Dai, H., de Sousa, P.J.F., Yin, B., 2012. On the numerical oscillation of the direct-forcing immersed-boundary method for moving boundaries. Comput. & Fluids 56, 61–76.

Luo, K., Wang, Z., Fan, J., Cen, K., 2007. Full-scale solutions to particle-laden flows: Multi-direct forcing and immersed boundary method. Phys. Rev. E 76, 066709.

Luo, L.S., Liao, W., Chen, X., Peng, Y., Zhang, W., 2011. Numerics of the lattice Boltzmann method: Effects of collision models on the lattice Boltzmann simulations. Physical Review E 83, 1–24.

Luo, X., Cai, Z., Li, W., Pedley, T., 2008. The cascade structure of linear instability in collapsible channel flows. Journal of Fluid Mechanics 600, 45–76.

Ma, J., Wang, Z., Young, J., Lai, J.C.S., Sui, Y., Tian, F.B., 2020. An immersed boundary-lattice Boltzmann method for fluid-structure interaction problems involving viscoelastic fluids and complex geometries. J. Comput. Phys. 415, 109487.

Malek, A.M., Alper, S.L., Izumo, S., 1999. Hemodynamic shear stress and its role in atherosclerosis. JAMA 282, 2035–2042.

Marzo, A., Luo, X., Bertram, C., 2005. Three-dimensional collapse and steady flow in thick-walled flexible tubes. J. Fluids Struct. 20, 817–835.

Mazharmanesh, S., Stallard, J., Medina, A., Fisher, A., Ando, N., Tian, F.B., Young, J., Ravi, S., 2021. Effects of uniform vertical inflow perturbations on the performance of flapping wings. Royal Society Open Science 8, 210471. doi:10.1098/rsos.210471.

McCroskey, W.J., 1982. Unsteady airfoils. Annual Review of Fluid Mechanics 14, 285–311. doi:doi:10.1146/annurev.fl.14.010182.001441.

Menon, K., Mittal, R., 2019. Flow physics and dynamics of flow-induced pitch oscillations of an airfoil. Journal of Fluid Mechanics 877, 582–613. doi:10.1017/jfm.2019.627.

Mittal, R., Bhardwaj, R., 2022. Immersed boundary methods for thermofluids problems. Annu. Rev. Heat Transf. 24, 33–70.

Mittal, R., Dong, H., Bozkurttas, M., Najjar, F., Vargas, A., Von Loebbecke, A., 2008. A versatile sharp interface immersed boundary method for incompressible flows with complex boundaries. J. Comput. Phys. 227, 4825–4852.

Mittal, R., Iaccarino, G., 2005. Immersed boundary methods. Annu. Rev. Fluid Mech. 37, 239–261.

Mittal, R., Seo, J.H., Vedula, V., Choi, Y.J., Liu, H., Huang, H.H., Jain, S., Younes, L., Abraham, T., George, R.T., 2016. Computational modeling of cardiac hemodynamics: current status and future outlook. J. Comput. Phys. 305, 1065–1082.

Mohd-Yusof, J., 1997. Combined immersed-boundary/b-spline methods for simulations of flow in complex geometries. Center for turbulence research annual research briefs 161, 317–327.

Ol, M.V., Eldredge, J.D., Lian, Y., Garmann, D.J., Altman, A., 2010. Résumé of the AIAA FDTC Low Reynolds Number Discussion Group's Canonical Cases, in: 48th AIAA Aerospace Sciences Meeting, American Institute of Aeronautics and Astronautics, Inc.. pp. 1–18.

Peng, C., Wang, L.P., 2020. Force-amplified, single-sided diffused-interface immersed boundary kernel for correct local velocity gradient computation and accurate no-slip boundary enforcement. Phys. Rev. E 101, 053305.

Peskin, C.S., 1972. Flow patterns around heart valves: a numerical method. J. Comput. Phys. 10, 252–271.

Peskin, C.S., 2002. The immersed boundary method. Acta Numerica 11, 479–517.

Sane, S.P., Dickinson, M.H., 2001. The control of flight force by a flapping wing: lift and drag production. Journal of Experimental Biology 204, 2607–2626. doi:10.1242/jeb.204.15.2607.

Sane, S.P., Dickinson, M.H., 2002. The aerodynamic effects of wing rotation and a revised quasi-steady model of flapping flight. Journal of Experimental Biology 205, 1087–1096. doi:https://doi.org/10.1242/jeb.205.8.1087.

Seo, J.H., Mittal, R., 2011. A sharp-interface immersed boundary method with improved mass conservation and reduced spurious pressure oscillations. J. Comput. Phys. 230, 7347–7363.

Song, J., Luo, H., Hedrick, T.L., 2014. Three-dimensional flow and lift characteristics of a hovering ruby-throated hummingbird. J. R. Soc. Interface 11, 20140541.

Sotiropoulos, F., Yang, X., 2014. Immersed boundary methods for simulating fluid–structure interaction. Prog. Aerosp. Sci. 65, 1–21.

Sui, Y., Chew, Y.T., Roy, P., Low, H.T., 2007. A hybrid immersed-boundary and multi-block lattice Boltzmann method for simulating fluid and moving-boundaries interactions. Int. J. Numer. Methods Fluids 53, 1727–1754.

Sum Wu, K., Nowak, J., Breuer, K.S., 2019. Scaling of the performance of insect-inspired passive-pitching flapping wings. Journal of The Royal Society Interface 16, 20190609. doi:10.1098/rsif.2019.0609.

Suzuki, K., Inamuro, T., 2011. Effect of internal mass in the simulation of a moving body by the immersed boundary method. Comput. Fluids 49, 173–187.

Tao, S., He, Q., Chen, J., Chen, B., Yang, G., Wu, Z., 2019a. A non-iterative immersed boundary-lattice Boltzmann method with boundary condition enforced for fluid–solid flows. Appl. Math. Model. 76, 362–379.

Tao, S., He, Q., Wang, L., Huang, S., Chen, B., 2019b. A non-iterative direct-forcing immersed boundary method for thermal discrete unified gas kinetic scheme with dirichlet boundary conditions. Int. J. Heat Mass Transf. 137, 476–488.

Tian, F.B., Dai, H., Luo, H.X., Doyle, J.F., Rousseau, B., 2014a. Fluid–structure interaction involving large deformations: 3D simulations and applications to biological systems. Journal of Computational Physics 258, 451–469.

Tian, F.B., Luo, H., Zhu, L., Liao, J.C., Lu, X.Y., 2011. An efficient immersed boundary-lattice Boltzmann method for the hydrodynamic interaction of elastic filaments. J. Comput. Phys. 230, 7266–7283.

Tritton, D.J., 1959. Experiments on the flow past a circular cylinder at low reynolds numbers. Journal of Fluid Mechanics 6, 547–567.

Truong, Q.T., Nguyen, Q.V., Truong, V.T., Park, H.C., Byun, D.Y., Goo, N.S., 2011. A modified blade element theory for estimation of forces generated by a beetle-mimicking flapping wing system. Bioinspiration & Biomimetics 6, 036008. doi:10.1088/1748-3182/6/3/036008.

Turek, S., Hron, J., 2006. Proposal for numerical benchmarking of fluid-structure interaction between an elastic object and laminar incompressible flow, in: Fluid-Structure Interaction, Springer Berlin Heidelberg. pp. 371–385.

Walker, J.M., Helin, H.E., Strickland, J.H., 1985. An experimental investigation of an airfoil undergoing large-amplitude pitching motions. AIAA Journal 23, 1141–1142. doi:10.2514/3.9055.

Wang, L., Currao, G., Han, F., Neely, A., Young, J., Tian, F.B., 2017. An immersed boundary method for fluid–structure interaction with compressible multiphase flows. J. Comput. Phys. 346, 131–151.

Wang, L., Tian, F.b., 2019. Numerical simulation of flow over a parallel cantilevered flag in the vicinity of a rigid wall. Phys. Rev. E 99.

Wu, J., Shu, C., 2009. Implicit velocity correction-based immersed boundary-lattice Boltzmann method and its applications. Journal of Computational Physics 228, 1963–1979.

Wu, J., Shu, C., 2010. An improved immersed boundary-lattice boltzmann method for simulating three-dimensional incompressible flows. J. Comput. Phys. 229, 5022–5042.

Xu, L., Tian, F.B., Young, J., Lai, J.C.S., 2018. A novel geometry-adaptive Cartesian grid based immersed boundary–lattice Boltzmann method for fluid–structure interactions at moderate and high Reynolds numbers. J. Comput. Phys. 375, 22–56.

Yu, D., Mei, R., Shyy, W., 2002. A multi-block lattice Boltzmann method for viscous fluid flows. International journal for numerical methods in fluids 39, 99–120.

Zhang, C., Cheng, Y., Zhu, L., Wu, J., 2016. Accuracy improvement of the immersed boundary-lattice Boltzmann coupling scheme by iterative force correction. Comput. Fluids 124, 246–260.

Zhang, C., Rezavand, M., Hu, X., 2021. A multi-resolution sph method for fluid-structure interactions. J. Comput. Phys. 429, 110028.

Zhang, S., Luo, X.Y., Cai, Z., 2018. Three-dimensional flows in a hyperelastic vessel under external pressure. Biomech. Model. Mechanobiol. 17, 1187–1207.

Zhang, Y., Pan, G., Zhang, Y., Haeri, S., 2020. A relaxed multi-direct-forcing immersed boundary-cascaded lattice Boltzmann method accelerated on GPU. Comput. Phys. Commun. 248, 106980.

Zhao, X., Chen, Z., Yang, L., Liu, N., Shu, C., 2021. Efficient boundary condition-enforced immersed boundary method for incompressible flows with moving boundaries. J. Comput. Phys. , 110425.

Zhu, C., Li, G., Luo, H., 2014. A high-order immersed-boundary method for simulations of flapping wings, in: 32nd AIAA Applied Aerodynamics Conference, p. 2148.

Zhu, L., 2018. A three-dimensional immersed boundary method for non-Newtonian fluids. Theor. Appl. Mech. Lett. 8, 193–196.

Zhu, Y., Tian, F.B., Young, J., Liao, J.C., Lai, J.C.S., 2021. A numerical study of fish adaption behaviors in complex environments with a deep reinforcement learning and immersed boundary–lattice Boltzmann method. Sci. Rep. 11, 1–20.

3 Performance Metric

3.1 Peer-reviewed Journal and Conference Papers

1. Huang, Q., Liu, Z., Wang, L., Ravi, S., Young, J., Lai, J.C.S. and Tian, F.-B. (2022) Streamline penetration, velocity error and consequences of the feedback immersed boundary method. Physics of Fluids, 34(9), 097101.

2. Huang, Q., Tian, F.-B., Young, J., Lai, J.C.S. and Ravi, S. (2022) Numerical modelling of under-actuated flapping wings inspired by the indirect-flight muscles of insects. 23rd Australasian Fluid Mechanics Conference

3. Bhat, S. S., Mazharmanesh, S., Medina, A. and Ravi, S. (2022) Effects of pitch perturbations on a rotating wing. 23rd Australasian Fluid Mechanics Conference, Sydney, Australia, Dec. 4–8, 2022.

4. Huang, Q., Tian, F.-B., Young, J., Lai, J.C.S. and Ravi, S. (2023) Numerical study of passively pitching tandem dragonfly wings for hovering flight. AIAA SciTech (accepted)

5. Huang, Q., Bhat, S. S., Yeo, E., Young, J., Lai, J.C.S., Tian, F.-B. and Ravi, S. (2023) Power synchronisations determine the hovering flight efficiency of passively pitching flapping wings. Journal of Fluid Mechanics (Under consideration for publication)